# PARTICLE IDENTIFICATION WITH THE ND280 FINE GRAINED DETECTORS FOR THE T2K EXPERIMENT

## A Thesis

Submitted to the Faculty of Graduate Studies and Research

In Partial Fulfillment of the Requirements

For the Degree of

Master of Science

in

Physics

University of Regina

by

Anezka Popovski Kolaceke

Regina, Saskatchewan

September, 2014

Copyright 2014: A. P. Kolaceke

#### **ABSTRACT**

The main goal of this thesis is the development of an algorithm for identification of particles (protons, electrons, muons and pions) with trajectories contained within the Fine Grained Detectors of the T2K (Tokai-to-Kamioka) experiment. This is achieved by constructing a distribution that compares the distance and the energy deposited by a particle travelling in the detectors. Using this distribution, a probability density function is created using simulations for particles interacting in the FGDs. The method of comparison includes the calculation of the pull variable, which gives a measurement of how close a particle being analysed is to a determined particle hypothesis. These pull variables can then be used as an estimate of the likelihood for the particle identification. Tests using this method were performed using an independent set of simulated samples, and also control samples of real protons and muons collected with the experiment. The results show that protons and electrons can be identified successfully from muons and pions. However, the developed particle identification algorithm is unable to discriminate between muons and pions since they behave in a very similar way under the conditions studied.

#### **ACKNOWLEDGEMENTS**

I would like to thank my supervisor, Mauricio Barbi, for all the help and patience during the development of this project, and also for all the opportunities given to me.

I would also like to thank all the T2K Canada members for the support, especially the Regina group – Dr. Edward Mathie, Dr. Roman Tacik, and Dr. Nick Hasting, and my graduate student colleagues Caio Licciardi and Spencer Giffin. All the help and discussions were fundamental for the conclusion of this thesis.

I also acknowledge the Department of Physics at the University of Regina for all the support, and the Faculty of Graduate Studies and Research for the partial funding through many teaching assistantships, an International Graduate Student Scholarship and a Graduate Research Award.

I need to thank all my friends for the support, fun and chatting. A special thanks goes to my friend Erica Partridge for everything. It is always good to know that you have someone you can count on.

Finally, I would like to thank my family, Cristina, Estanislao and Andrei for, in spite of the distance, still support me in all my decisions. I love you guys!

# TABLE OF CONTENTS

ABSTRACT	i
ACKNOWLEDGEMENTS	ii
TABLE OF CONTENTS	iii
LIST OF TABLES	v
LIST OF ILLUSTRATIONS	vi
LIST OF ABBREVIATIONS	xii
NTRODUCTION	1
CHAPTER ONE: Theoretical Considerations	3
1.1 Neutrinos	3
1.2 The T2K Experiment	11
1.3 Fine Grained Detectors	15
CHAPTER TWO: Interactions between Particles and Matter	20
2.1 Introduction	20
2.2 Scintillator detectors	23
CHAPTER THREE: Methodology	25
3.1 PDFs development	25
3.2 Energy and track length	29
3.3 Probability density functions	41

3.4 Likelihood analysis	43
CHAPTER FOUR: Results	50
4.1 Pull results	50
4.2 Results using real data	58
CHAPTER FIVE: Conclusions	66
BIBLIOGRAPHY	68
APPENDIX A	71

# LIST OF TABLES

Table 3.1: Number of particles used in generation of the PDFs for FGD1 28
Table 3.2: Number of particles used in generation of the PDFs for FGD2 28
Table 3.3: Fitting parameters using eq. 3.3 for the PDFs in FGD1 (fig. 3.25) 47
Table 3.4: Fitting parameters using eq. 3.3 for PDFs in FGD2 (fig. 3.26) 48
Table 3.5: Fitting parameters using eq. 3.4 in standard deviation for FGD1 (Fig
3.27)
Table 3.6: Fitting parameters using eq. 3.4 in standard deviation for FGD2 (Fig
3.28)

# LIST OF ILLUSTRATIONS

Figure 1.1: Beta decay3
Figure 1.2: Inverse beta decay4
Figure 1.3: "Standard Model of elementary particles" by MissMJ6
Figure 1.4: Contribution from different processes for energy production in stars
with different core temperatures7
Figure 1.5: The CNO cycle7
Figure 1.6: Main form of pp chain in the Sun8
Figure 1.7: Solar neutrino spectrum as predicted by the standard solar model 9
Figure 1.8: Sketch of the location of each of the T2K experiment components 12
Figure 1.9: Schematic of the neutrino beamline12
Figure 1.10: Effect of the off-axis beam technique relative to the neutrino energy
spectrum and compared to the oscillation probability curve
Figure 1.11: Off-axis near detector in T2K15
Figure 1.12: View of FGD with its scintillator bar modules stacked
Figure 1.13: Cross-section of a FGD scintillator bar
Figure 1.14 – Scintillator bars with WLS fiber in its center, connected to MPPC.18
Figure 1.15: Representation of a charged-current quasi elastic reaction, where a
muon neutrino interacts with a neutron, producing a muon and a proton 19

Figure 2.1: Ionization energy loss for charged pions, muons and protons in an
organic scintillator22
Figure 3.1: Representation of fiducial volume region relative to FGD
Figure 3.2: Representation of the coordinate axes relative to the neutrino beam
direction in the ND280 detector. 27
Figure 3.3: 2-dimensional representation of the angular bins used in the
simulations
Figure 3.6: Correlation between energy and track length for electrons in FGD1
using_truth (left-hand side) and reconstructed (right-hand side) variables 30
Figure 3.7: Correlation between energy and track length for pions in FGD1 using
truth (left-hand side) and reconstructed (right-hand side) variables 31
Figure 3.8: Correlation between energy and track length for protons in FGD1 with
angles smaller than 70°
Figure 3.9: Correlation between energy and track length for muons in FGD1 with
angles smaller than 70°
Figure 3.10: Correlation between energy and track length for electrons in FGD1
with angles smaller than 70°
Figure 3.11: Correlation between energy and track length for pions in FGD1 with
angles smaller than 70°
Figure 3.12: Correlation between energy and track length for protons in FGD2
with angles smaller than 70°34
Figure 3.13: Correlation between energy and track length for muons in FGD2
with angles smaller than 70°

Figure 3.14: Correlation between energy and track length for electrons in FGI	<b>D</b> 2
with angles smaller than 70°	35
Figure 3.15: Correlation between energy and track length for pions in FGD2 w	ith
angles smaller than 70°	35
Figure 3.16: Energy distribution for protons (top left), muons (top right), electron	ns
(bottom left) and pions (bottom right) in FGD1.	36
Figure 3.17: Energy distribution for protons (top left), muons (top right), electron	ns
(bottom left) and pions (bottom right) in FGD2.	37
Figure 3.18: Difference in energy between reconstructed and true energy f	for
simulated protons (top left), muons (top right), electrons (bottom left) and pio	ns
(bottom right) in FGD1.	38
Figure 3.19: Track length distribution for protons (top left), muons (top righ	ıt),
electrons (bottom left) and pions (bottom right) in FGD1	39
Fig. 3.20: Track length distribution for protons (top left), muons (top righ	ıt),
electrons (bottom left) and pions (bottom right) in FGD2	40
Figure 3.21: PDF for protons (top left), muons (top right), electrons (bottom le	eft)
and pions (bottom right) in FGD1.	42
Figure 3.22: PDF for protons (top left), muons (top right), electrons (bottom le	∍ft)
and pions (bottom right) in FGD2.	43
Fig. 3.23: PDF fittings for protons (top left), muons (top right), electrons (botto	mc
left) and pions (bottom right) in FGD1.	45
Fig. 3.24: PDF fittings for protons (top left), muons (top right), electrons (botto	mc
left) and pions (bottom right) in FGD2.	46

Fig. 3.25: Standard deviation fittings for protons (top left), muons (top right),
electrons (bottom left) and pions (bottom right) in FGD1
Fig. 3.26: Standard deviation fittings for protons (top left), muons (top right),
electrons (bottom left) and pions (bottom right) in FGD2
Figure 4.1: Pull distributions for each particle hypothesis assuming a pure proton
sample in FGD151
Figure 4.2: Pull distributions for each particle hypothesis assuming a pure muon
sample in FGD151
Figure 4.3: Pull distributions for each particle hypothesis assuming a pure
electron sample in FGD152
Figure 4.4: Pull distributions for each particle hypothesis assuming a pure pion
sample in FGD152
Figure 4.5: Pull distributions for each particle hypothesis assuming a pure proton
sample in FGD253
Figure 4.6: Pull distributions for each particle hypothesis assuming a pure muon
sample in FGD253
Figure 4.7: Pull distributions for each particle hypothesis assuming a pure
electron sample in FGD254
Figure 4.8: Pull distributions for each particle hypothesis assuming a pure pion
sample in FGD254
Figure 4.9: Pull distributions for proton (top left), muon (top right), electron
(bottom left) and pion (bottom right) samples in FGD1 using the combined
method 55

Figure 4.10: Pull distributions for proton (top left), muon (top right), electron
(bottom left) and pion (bottom right) samples in FGD2 using the combined
method
Figure 4.11: Likelihood for different particle hypotheses for sample of protons
(top left), muons (top right), electrons (bottom left) and pions (bottom right) in
FGD157
Figure 4.12: Likelihood for different particle hypotheses for sample of protons
(top left), muons (top right), electrons (bottom left) and pions (bottom right) in
FGD2
Figure 4.13: Pull distribution for proton, muon, electron and pion hypotheses
when applied to stopping proton data sample in FGD160
Figure 4.14: Pull distribution for proton, muon, electron and pion hypotheses
when applied to stopping proton data sample in FGD260
Figure 4.16: Comparison between pull distributions for simulated and real data
assuming the proton hypothesis for FGD1 61
Figure 4.17: Comparison between pull distributions for simulated and real data
assuming the proton hypothesis for FGD2 61
Figure 4.18: Pull distribution for proton, muon, electron and pion hypotheses
when applied to stopping muon data sample in FGD163
Figure 4.19: Pull distribution for proton, muon, electron and pion hypotheses
when applied to stopping muon data sample in FGD2 64
Figure 4.20: Comparison between pull distributions for simulated and real data
using muon hypothesis and muon sample for FGD164

Figure	4.21: (	Comparison	between	pull	distributions	for	simulated	and	real	data
using r	muon h	ypothesis ar	nd muon s	amp	le for FGD2					65

## LIST OF ABBREVIATIONS

**ADC** Analog-to-digital converter

**CNO** Carbon-nitrogen-oxygen

**CP** Charge Parity

**DONUT** Direct Observation of the Nu Tau

**ECal** Electromagnetic Calorimeter

**FGD** Fine Grained Detector

**J-PARC** Japan Proton Accelerator Research Complex

KamLAND Kamioka Liquid Scintillator Antineutrino Detector

**LINAC** Linear Accelerator

MPPC Multi-Pixel Photo Counter

MR Main ring

ND280 Near detector 280 m

**P0D** Pi-zero Detector

**PDF** Probability density function

**p.e.** photoelectron

**PID** Particle Identification

**POPOP** 1,4-bis (5-phenuloxazol-2-yl) benzene  $\{C_{24}H_{16}N_2O_2\}$ 

**PPO** 2,5-diphenyloxazole {C<sub>15</sub>H<sub>11</sub>NO}

**PS** polystyrene

PVT polyvinyltoluene

**RCS** Rapid Cycling Synchrotron

**SM** Standard Model

**SMRD** Side Muon Range Detector

**SNO** Sudbury Neutrino Observatory

SK Super Kamiokande

T2K Tokai-to-Kamioka

**TPC** Time Projection Chamber

**UV** ultraviolet

WLS wavelength shifting

#### INTRODUCTION

Since the suggestion and first experimental evidences of neutrino oscillations, many experiments were designed to prove their existence and measure parameters associated with this phenomenon. A full description of the neutrino oscillations will not only shed light over the physical behaviour of neutrinos, which are particles very difficult to detect and, therefore, study, because of its properties (see section 1.1 for more details), but can also lead to a better understanding of the CP (charge parity) violation, which might ultimately explain why the Universe is mainly formed by matter instead of antimatter.

The T2K (Tokai-to-Kamioka) experiment is one of many attempts to understand neutrino oscillations. It is composed of three main parts, neutrino beamline; ND280, a near detector, localized 280 m away from the target; and Super-Kamiokande, a far detector located at 295 km from the beam target (for more details, refer to section 1.2).

The main goal of this thesis was the development of a particle identification algorithm for the Fine Grained Detectors (FGDs), which are part of the ND280. The algorithm should be able to work with electrons, protons, muons and pions whose trajectories start and stop within the FGDs.

The thesis is divided in five chapters, besides this introduction. Chapter one discusses theoretical aspects of neutrino physics (section 1.1) and gives details about the T2K experiment (section 1.2) and FGDs (section 1.3). Chapter two talks about the theory of interactions between particles and matter in general and the laws governing its principles (section 2.1) and the specifics of scintillator detectors (section 2.2). The

methodology used is described in Chapter three, where the simulation parameters for the particles used to build the probability density functions (section 3.1), the analysis of the simulated sample (sections 3.2), the generation of probability density functions (section 3.3) and the likelihood analysis (section 3.4) are explained. Chapter four discusses the results obtained with this algorithm, first using a second set of simulated particles (section 4.1), and then applying the algorithm to real data obtained in the detector and previously identified by other detectors in ND280 (section 4.2). Finally, Chapter five shows the conclusions obtained in this thesis work.

#### **CHAPTER ONE: Theoretical Considerations**

#### 1.1 Neutrinos

The existence of neutrinos was first suggested in 1930 after the unsuccessful description of beta decays. It was believed that in negative beta decay processes, a nucleus would decay into another nucleus (the latter with an extra proton) and an electron. The problem is that, in two-body decays, each produced particle should have a well-defined energy following the energy and momentum conservation laws, whereas the measured particles in those experiments had unpredicted energy distributions. Wolfgang Ernst Pauli proposed that another particle, electrically neutral and extremely light (or massless), was also emitted [1]. This particle was escaping detection, and thus partially carrying away undetected energy and momentum of the system. Following up with Pauli's proposal, Enrico Fermi called this particle neutrino (v) [1][2]. The beta-decay was then described as the emission of an electron (or positron) and an anti-neutrino (neutrino) by a nucleus, as depicted in fig. 1.1 [3].



Figure 1.1: Beta decay. Figure reproduced from OpenStax College "Nuclear Decay and Conservation Laws (http://cnx.org/content/m42633/1.6/) licensed under CC-BY 3.0. (Original in colour.)

The road for the detection of neutrinos was a long one. The main reason being the fact that neutrinos are very weakly interacting particles, making them difficult to detect.

The first neutrino was only identified in 1955 in an experiment carried out by C.L. Cowan et al. using inverse beta-decay (fig. 1.2) [4]. This neutrino was associated to electrons, and is now known as electron-neutrino.

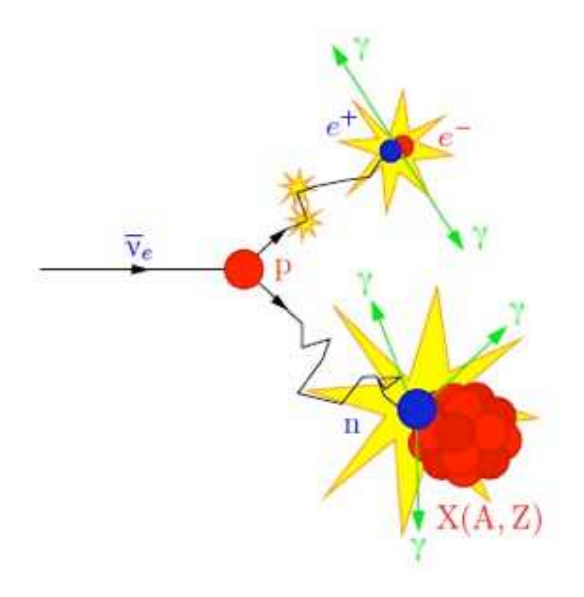


Figure 1.2: Inverse beta decay. Figure obtained from Quantum Diaries (http://www.quantumdiaries.org). Reproduced with permission. (Original in colour.)

By then, physicists knew that neutrinos existed, but only one type was known so far. The first experiment to test the hypothesis of the existence of two kinds of neutrino was developed in 1962 by Leon M. Lederman, Melvin Shwartz and Jack Steinberger [1][5]. In this experiment, they used anti-neutrinos originated from pion decays, which now is known to take the form:

$$\pi^- \to \mu^- + \bar{\nu}_{\mu}$$
 (1.1).

They identified 29 events compatible with the following reaction:

$$\bar{\nu}_{\mu} + p^{+} \to \mu^{+} + n$$
 (1.2).

On the other hand, none following the reaction below was identified:

$$\bar{\nu}_{\mu} + p^{+} \to e^{+} + n$$
 (1.3).

Reaction (1.3) is now known to be forbidden [1]. Thus the conclusion was that there should be another type of neutrino for this result to be possible: the muon-neutrino.

When the third lepton, tau, was discovered in 1975 by M. L. Perl *et al.* [6], it was implicit that a new type of neutrino should exist, since there was a neutrino for each of the lepton generations (see next paragraph) known to date (electron and muon generations). As it was expected, the tau-neutrino was directly observed 26 years later, in 2001, by the Direct Observation of the Nu Tau (DONUT) collaboration [7].

With three lepton generations, the lepton classification in the Standard Model (SM) of particle physics was complete. In this model, the particles are separated in families of quarks, leptons and the mediators of the fundamental forces (weak, strong and electromagnetic). The lepton and quark families are grouped in generations constituted of pairs of particles with similar characteristics. The mediators are bosons responsible for the interactions among particles: photons for the electromagnetic force; gluons for the strong force; and the W<sup>+</sup>, W<sup>-</sup> and Z bosons for the weak force [1]. The families and generations of the SM are represented in fig. 1.3. Until recently, neutrinos were assumed to be massless particles in the SM. However, this assumption was already been challenged since the first observations of what is known as the "solar neutrino problem"

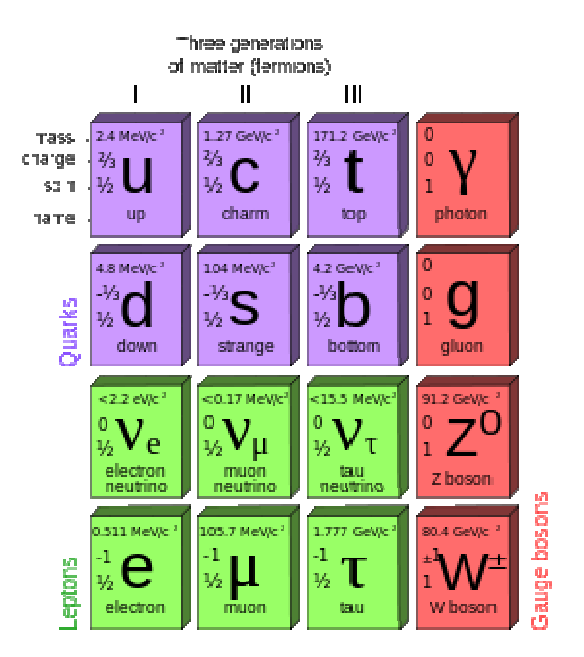


Figure 1.3: "Standard Model of elementary particles" by MissMJ is licensed under CC BY 3.0 (http://commons.wikimedia.org/wiki/File:Standard\_Model\_of\_Elementary\_Particles.svg) (Original in colour.)

The processes of energy generation in stars depend on their masses. For heavier stars, with temperature above 20 million degrees (see fig. 1.4), the dominant mechanism is the carbon-nitrogen-oxygen (CNO) cycle as shown in fig. 1.5 [8]. In this process, nuclear fusion is catalyzed by these elements [1]. The main reaction steps are [8]:

$$^{12}C + p \rightarrow ^{13}N + \gamma$$
 $^{13}N \rightarrow ^{13}C + e^{+} + \nu_{e}$   $(E_{\nu} \leq 1.2 \text{ MeV})$ 
 $^{13}C + p \rightarrow ^{14}N + \gamma$ 
 $^{13}N + p \rightarrow ^{15}O + \gamma$ 
 $^{15}O \rightarrow ^{15}N + e^{+} + \nu_{e}$   $(E_{\nu} \leq 1.73 \text{ MeV})$ 
 $^{15}N + p \rightarrow ^{12}C + ^{4}He$ 

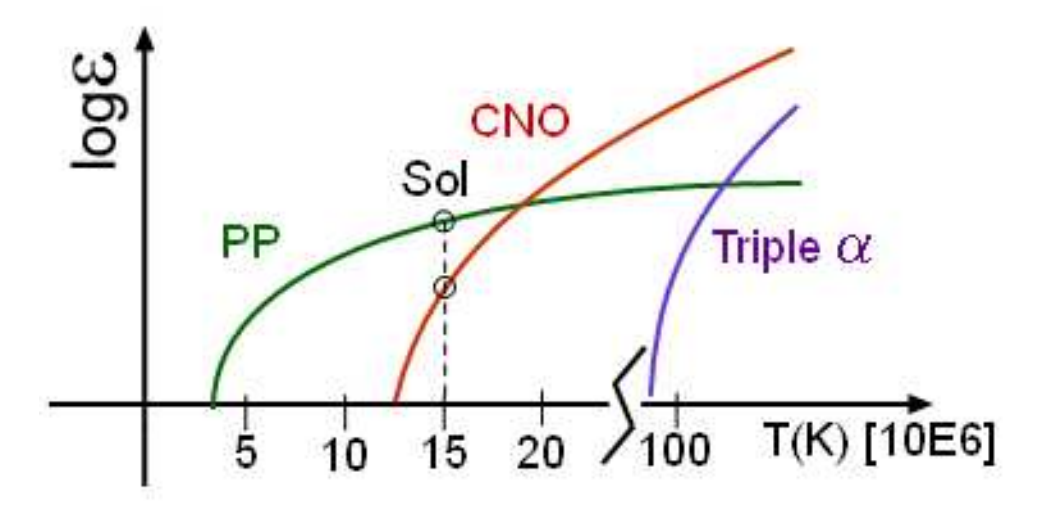


Figure 1.4: Contribution from different processes for energy production in stars with different core temperatures. Heavier stars have higher temperatures. Original by Orgullobot, licensed under GNU Free Documentation License. (Original in colour.).

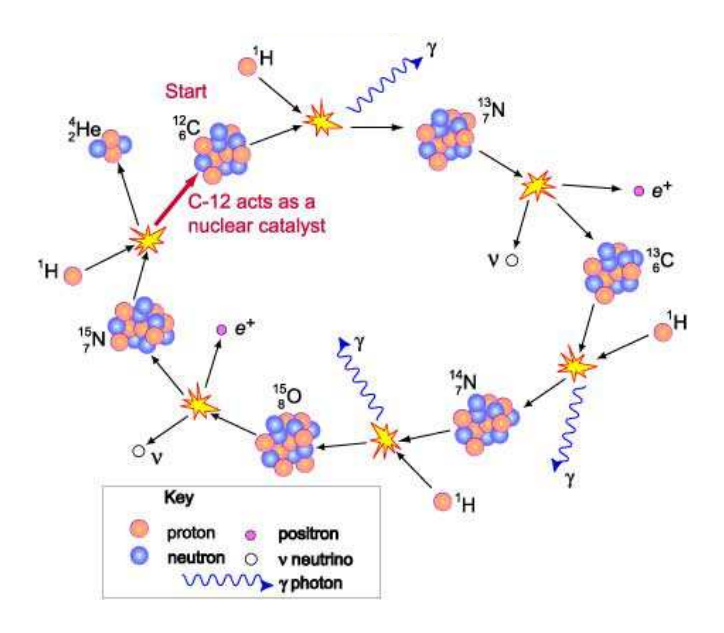


Figure 1.5: The CNO cycle. Picture from Australia Telescope Outreach and Education (http://outreach.atnf.csiro.au/). Reproduced with permission. (Original in colour.)

In relatively lighter stars (such as the Sun, for instance), the dominant process is the pp chain (fig. 1.6) [1]. In this process, hydrogen nuclei (protons) combine forming

deuterons, which then combine with protons generating <sup>3</sup>He. The <sup>3</sup>He nuclei give birth to alpha particles (He nuclei) through reactions with protons, other alpha-particles and among themselves [1]. These reaction processes are well known, and each has a very characteristic energy spectrum, as shown in fig. 1.7.

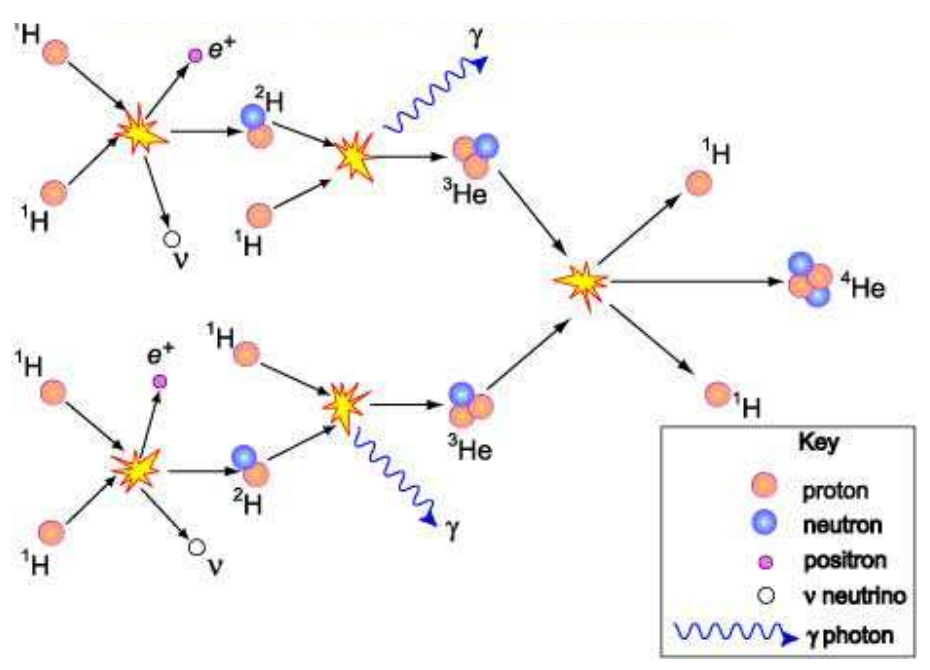


Figure 1.6: Main form of pp chain in the Sun. Picture from Australia Telescope Outreach and Education (http://outreach.atnf.csiro.au/). Reproduced with permission. (Original in colour.)

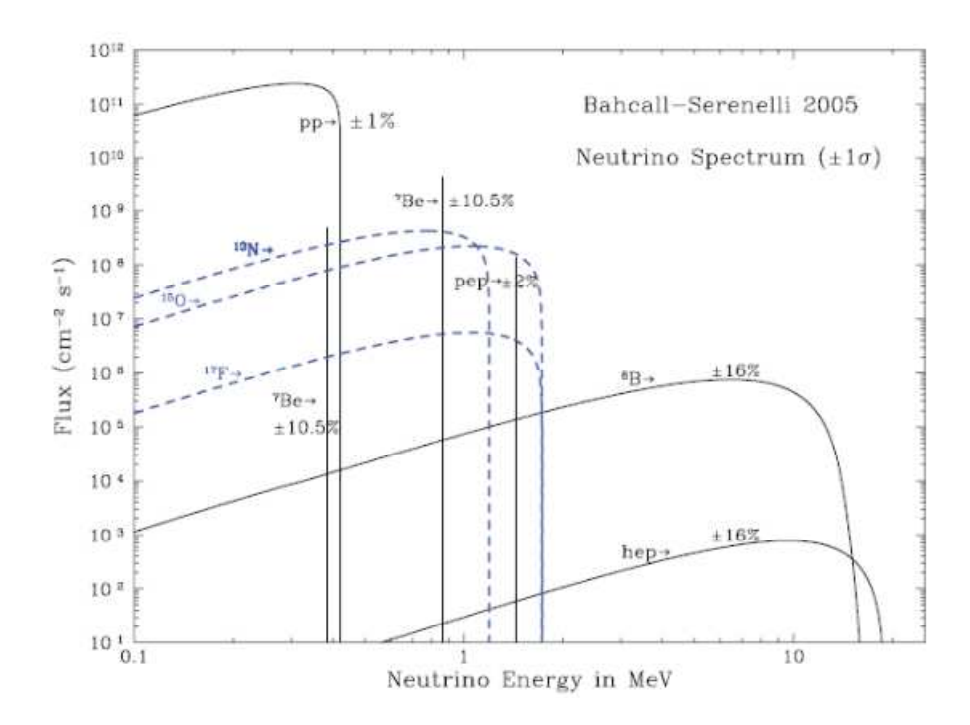


Figure 1.7: Solar neutrino spectrum as predicted by the standard solar model. Figure reproduced from [9].

The first experiments developed to measure solar neutrinos were reported in 1968 by Ray Davis, using a huge tank of chlorine [1], through the reaction [8]

$$^{37}Cl + \nu_e \rightarrow ^{37}Ar + e^-$$
 (1.4)

The results, however, were different from those expected for the total number of measured neutrinos was only about a third of that predicted using the accepted Solar Standard Model. This became known as the solar neutrino problem [1].

The solution came with the suggestion made by Bruno Pontecorvo in 1968 that neutrinos could oscillate among flavours in flight, for which Davis' experiment was not prepared, what is now called neutrino oscillation [1]. However, the oscillation can only occur if the neutrinos are massive [10].

The *n* flavour eigenstates  $|\nu_{\alpha}\rangle$ , with  $\langle \nu_{\beta} | \nu_{\alpha} \rangle = \delta_{\alpha\beta}$ , are given by a superposition of *n* mass eigenstates  $|\nu_{i}\rangle$  with  $\langle \nu_{i} | \nu_{j} \rangle = \delta_{ij}$ . Using a unitary mixing matrix U [10], these eigenstates can be written as:

$$|\nu_{\alpha}\rangle = \sum_{i} U_{\alpha i} |\nu_{i}\rangle$$
  $|\nu_{i}\rangle = \sum_{\alpha} (U^{\dagger})_{i\alpha} |\nu_{\alpha}\rangle = \sum_{\alpha} U^{*}_{\alpha i} |\nu_{\alpha}\rangle$  (1.5)

Where:

$$U^{\dagger}U = 1 \qquad \sum_{i} U_{\alpha i} U_{\beta i}^{*} = \delta_{\alpha \beta} \qquad \sum_{\alpha} U_{\alpha i} U_{\alpha j}^{*} = \delta_{ij} \qquad (1.6)$$

The mixing matrix can also be written in terms of three angles ( $\theta_{12}$ ,  $\theta_{23}$ ,  $\theta_{13}$ ) and one phase factor ( $\delta$ ):

$$U = \begin{pmatrix} c_{12}c_{13} & s_{12}c_{13} & s_{13}e^{-i\delta} \\ -s_{12}c_{23} - c_{12}s_{23}s_{13}e^{i\delta} & c_{12}c_{23} - s_{12}s_{23}s_{13}e^{i\delta} & s_{23}c_{13} \\ s_{12}s_{23} - c_{12}c_{23}s_{13}e^{i\delta} & -c_{12}s_{23} - s_{12}c_{23}s_{13}e^{i\delta} & c_{23}c_{13} \end{pmatrix}$$
(1.7)

where  $c_{ij} \equiv \cos \theta_{ij}$  and  $s_{ij} \equiv \sin \theta_{ij}$  [1].

The parameter  $\theta_{12}$  and  $\theta_{23}$  were first observed by the SNO (Sudbury Neutrino Observatory) in 2002 [11] and Super-Kamioka Neutrino Detection Experiment (Super-K) in 2003 [12], respectively. They are now given by  $\theta_{12} \approx \theta_{sol} = 34 \pm 2^{\circ}$  (for the solar neutrino oscillation) and  $\theta_{23} \approx \theta_{atm} = 45 \pm 8^{\circ}$  (for the atmospheric neutrino oscillation) [1]. The third angle,  $\theta_{13}$ , is known to be much smaller than the other two, and has been measured by T2K as  $\sin^2 2\theta_{13} = 0.140^{+0.038}_{-0.032}(0.170^{+0.045}_{-0.037})$  [13], and more precisely by the Daya Bay Reactor Neutrino Experiment as  $\sin^2 2\theta_{13} = 0.092 \pm 0.016(stat.) \pm 0.005$  (syst.) [14]. The measurement of this parameter was one of the main goals of the T2K experiment (see section 1.2). A non-zero value for  $\theta_{13}$  is a necessary condition for the existence of a non-zero CP-violation phase  $\delta$  [15]. This phase is of significant

importance as it can help understand the asymmetry between matter and anti-matter in the beginning of the Universe [1]. This asymmetry is the reason why the current Universe is completely dominated by matter.

## 1.2 The T2K Experiment

The T2K (Tokai-to-Kamioka) experiment is a long baseline neutrino experiment, designed to measure the  $\theta_{13}$  parameter through the measurement of electron-neutrino appearance from the muon-neutrino. In addition to sin this main goal, a highly accurate measurement of the parameter  $\theta_{23}$ , and the use of anti-neutrino beams so that the existence of a non-zero CP-violation phase can be explored are also key components of the T2K research program. The T2K also provides a rich environment for the development of studies in fixed-target physics neutrino interactions, at energies covering the transition between resonance production and deep inelastic scattering regimes [16], and for direct comparisons between neutrino/matter and antineutrino/matter interaction cross-sections.

The experiment is composed of a neutrino beamline (anti-neutrino beam mode can be achieved by inverting the polarity of some special magnets, called Horns [17]), a near detector complex at 280 m from the proton-target point both localized at the Japan Proton Accelerator Research Complex (J-PARC) in Tokai, and a far detector (Super-Kamiokande) at 295 km from the accelerator [16]. Fig. 1.8 is a sketch of the location of each of the T2K experiment components.

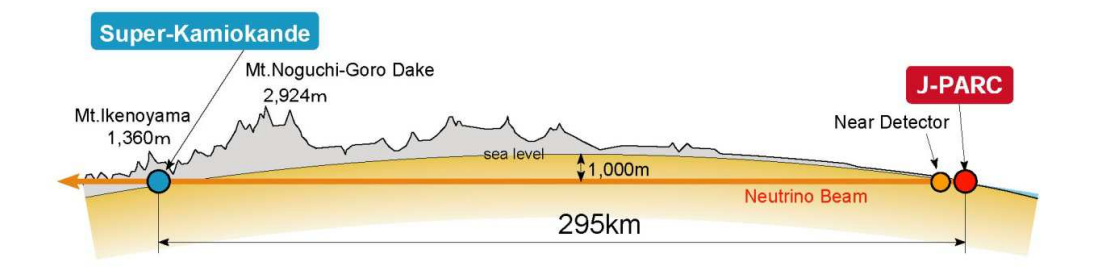


Figure 1.8: Sketch of the location of each of the T2K experiment components. (Original in colour.)

The J-PARC accelerator is composed by a linear accelerator (LINAC), a rapid-cycling synchrotron (RCS) and the main ring (MR), which result in a proton beam with energy up to 30 GeV separated in eight bunches in the MR. These eight bunches are extracted to the neutrino beamline by a set of five kicker magnets while still in a single turn in the MR. The neutrino beamline is composed by a primary beamline, which is responsible for setting the right direction for the beam (pointing towards Kamioka) and a secondary beamline, which takes the protons to the graphite target to generate secondary pions. These pions are focused by the Horns and decay into the neutrinos that compose the neutrino beam. A schematic diagram of the neutrino beamline can be seen in fig. 1.9 [16].

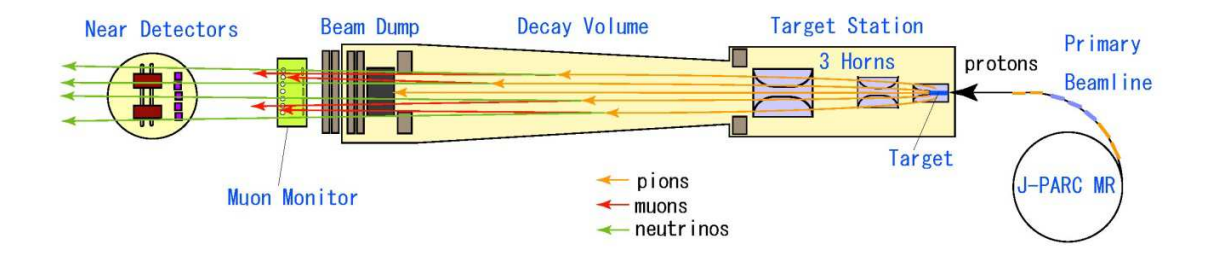


Figure 1.9: Schematic of the neutrino beamline. (Original in colour.)

The T2K neutrino beam is oriented at a 2.5° angle relative to the baseline connecting the proton target and the far detector (off-axis method). In this way, a very narrow-band-energy neutrino beam reaches the far detector, with a peak in energy at ~0.6 GeV, as can be seen in fig. 1.10. This method maximizes the neutrino oscillation at 295 km and minimizes the background [16].

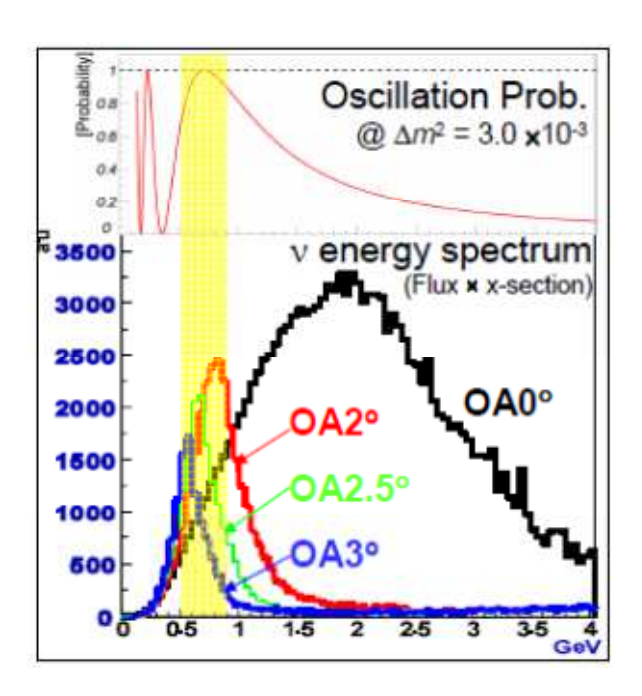


Figure 1.10: Effect of the off-axis beam technique relative to the neutrino energy spectrum and compared to the oscillation probability curve. (Original in colour.)

The near detector is composed of two complementary detectors: an on-axis detector (INGRID); and an off-axis detector (ND280). The INGRID detector is built as an array of iron/scintillator sandwiches, and is responsible for measuring the profile of the on-axis beam. It gives information on the beam direction, with a precision of 0.4 mrad, 280 m away from the beam origin, and on the beam intensity. The ND280 detector

is composed by a set of detectors immersed in a magnetic field. These detectors are responsible for measuring the muon-neutrino flux and the neutrino beam energy spectrum at 2.5 degrees, as well as contaminations from electron-neutrinos produced in the T2K decay volume that can potentially be misidentified as muon-neutrinos in the far detector [16].

The detectors composing the ND280 detector are shown in fig. 1.11 (see [16] provided for a detailed discussion and description of the structures of each detector). The ND280 is comprised of the following components:

- Pi-zero detector (P0D): responsible for measuring neutral current processes;
- Time Projection Chamber (TPC): responsible for identifying charged particles, and for measuring the three-momentum of each of these particles.
- Fine Grained Detector (FGD): responsible for providing a target mass for the neutrino interactions and for tracking the charged particles produced in the interaction. This detector will be discussed in more detail in the next section.
- Electromagnetic Calorimeter (ECal): responsible for measuring electromagnetic processes. It also provides coverage for particles exiting the ND280 detector.
- Side Muon Range Detector (SMRD): responsible for identifying muons at high angles relative to the neutrino beam direction that can escape. The SMRD measures the momentum of each muon. It is also fundamental in the triggering process to identify events coming from cosmic ray interactions, and for helping in the observation of beam-related interactions which happen in the surrounding of the detector and in the magnets.

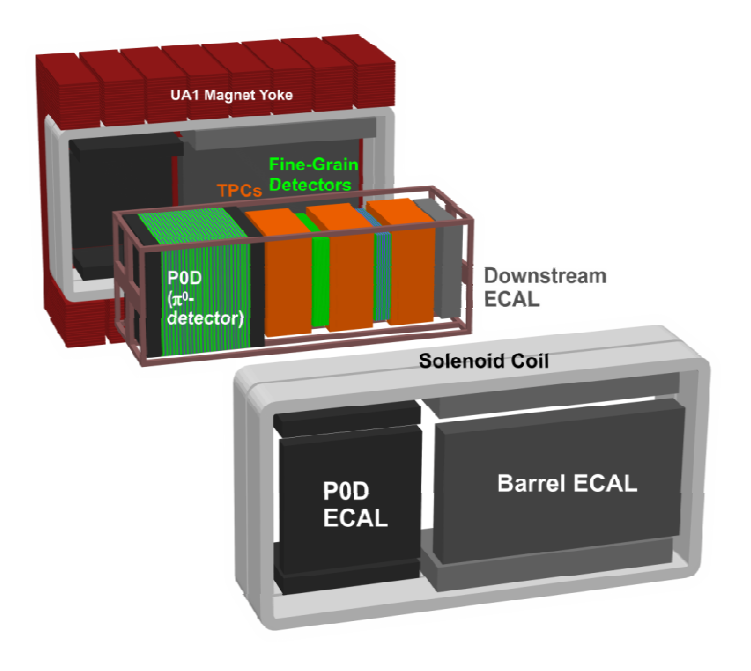


Figure 1.11: Off-axis near detector in T2K. (Original in colour.)

The far detector (Super-Kamiokande) is located at 1000 m under the rocks of the peak of Mount Ikenoyama. It is a Cherenkov detector based on water surrounded by approximately 13,000 photomultiplier tubes. The SK has been running since 1996, and was upgraded in 2005-06 for use in the T2K experiment [16].

#### 1.3 Fine Grained Detectors

The Fine Grained Detectors (FGDs) [18] are composed of 22 modules, each consisting of 192 horizontal and 192 vertical layers of 186.43 cm long scintillator bars as depicted in fig. 1.12. The bars are 1 cm x 1 cm in dimension (fig. 1.13), each containing a 191.5 cm long wavelength shifting (WLS) fibre through a 1.8 mm diameter axial hole. The WLS fibre-bar contact is through air. The bars are coated with a reflective 0.25 mm

thick layer of TiO<sub>2</sub>. Each WLS fibre is coupled on one of their sides to a photosensor, while the other side is coated with a reflective aluminum film deposited using a sputtering technique to enhance light yield.



Figure 1.12: View of FGD with its scintillator bar modules stacked. (Original in colour.)

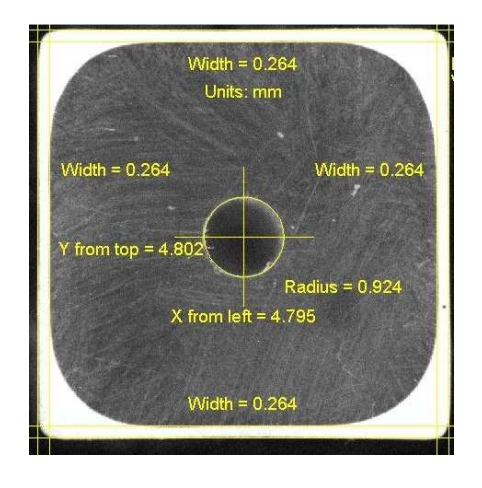


Figure 1.13: Cross-section of a FGD scintillator bar. (Original in colour.)

There are two FGD detectors, known as FGD1 and FGD2, with the FGD1 located more upstream relative to the neutrino beam direction than the FGD2. While the FGD1 contains fifteen scintillator bar modules, the FGD2 contains 7 scintillator bar modules interleaved by six water target modules [18]. The water modules serve as target for oxygen-neutrino interactions, which can be directly compared to carbon-neutrino interaction happening in the scintillator material. This is of importance to minimize systematic uncertainties when extrapolating the neutrino flux measured at the near detector to those measured using the far detector for the purpose of oscillation parameter measurements. The knowledge of the oxygen-neutrino interaction in the ND280 helps in this task because the SK detector is purely water-based. The water modules do not contain a readout system, but that is mitigated by the fact that the events happing in water are identified as excess in the neighbour scintillator bars. This allows a direct comparison between the interactions observed in the scintillator-based FGD1 (carbon-neutrino interactions) and the scintillator/water-based FGD2 (carbon-neutrino and oxygenneutrino interactions). All FGD modules are installed in a light-tight environment (dark box).

The photosensors used in the FGDs are the Multi-Pixel Photo Counters (MPPC) (fig. 1.14) produced by the Hamamatsu Company [19]. The MPPCs are silicon-based photosensors operated in the limited Geiger-mode [20]. Photons arriving on the MPPCs undergo photoelectron process. The electrons produced in these processes, known as photoelectrons (p.e.), are multiplied in each MPPC and output as charge current. The intensity of this current is proportional to the number of initial photons reaching the MPPCs and responsible for photoelectron processes. On the other hand, the number of

photons detected depends on the number of photons produced by a given particle-detector interaction. The latter is, in turn, dependent on the energy of this incident particle. Thus, knowing the output MPPC current, it is possible to reconstruct the original energy of the particle if a proper set of calibrations and corrections (such as for the number of photons attenuated in the WLS fibres) are applied. For this purpose, the output current of each MPPC is sent to an electronic system where the signal is digitalized and prepared to be stored in a computer farm, where further treatment is applied as the data is prepared for processing (reconstruction). The FGD's front-end electronics are organized in 24 minicrates, each attached to the four sides of the FGD dark box. The signals coming from the MPPCs are transferred to the electronics through ribbon cables attached to the crates' backplanes [18].



Figure 1.14 – Scintillator bars with WLS fiber in its center, connected to MPPC. (Original in colour.)

The mini-crates are cooled by a sub-atmospheric pressure water cooling system that runs on the sides of the dark box frame. Every piece of heat-producing electronics is located outside of the box, while only elements with almost no power dissipation, as are the photosensors, stay inside the box [18].

The FGDs and TPCs form the ND280 Tracker and, together, they are the main responsible for identifying and measuring charged-current quasi elastic (CCQE) reactions (see fig. 1.15), the main reaction taken into account during T2K analysis. For these events, particle identification is typically performed by the TPCs, but when particles stop within the FGD, this is not possible. In this case, it is important that FGDs can identify particles fully contained in their volume, which is the topic of this thesis.

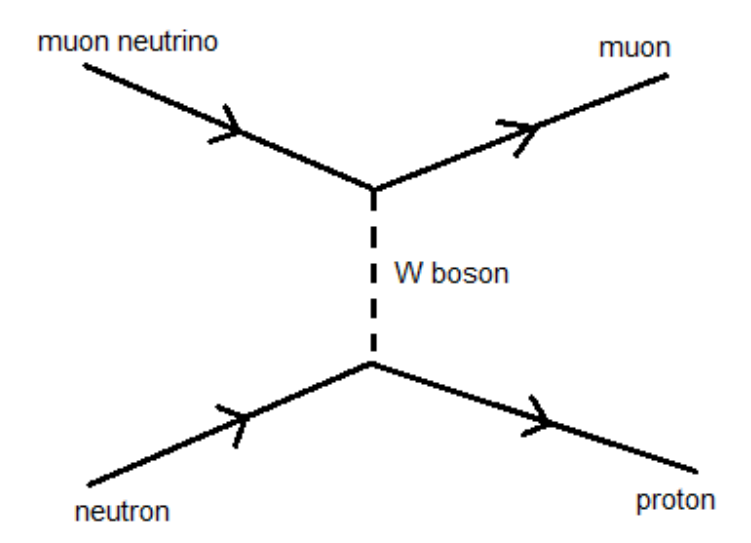


Figure 1.15: Representation of a charged-current quasi elastic reaction, where a muon neutrino interacts with a neutron, producing a muon and a proton.

#### **CHAPTER TWO: Interactions between Particles and Matter**

#### 2.1 Introduction

A particle needs to interact with the material of the detector to be detected. In other words, what is observed from a detector is not the particle *per se* but the result of its interaction with the matter that makes the detector. A detailed discussion of the interaction between particles and matter can be found in [21]. The intention of this chapter is to summarize some relevant points found in that reference, which were found to be useful for the development of this thesis. Further references will be cited when appropriate.

There are two kinds of possible interactions between particles and matter:

- 1. "short-range interactions", when the particle interacts with the atomic nucleus in the detector matter:
- 2. "long-range electromagnetic interactions", including "ionization energy losses", when particles lose energy to matter through ionization, and "radiation energy losses", when particles emit radiation.

At the energy range of interest (energies up to 500 MeV), the ionization energy losses are dominant for all charged particles except electrons and positrons.

The ionization energy losses are mostly due to Coulomb scatterings due to the interactions of the incident particles with atomic electrons found in the material. A theory to explain such losses was developed in the 1930s by Hans Bethe, Felix Bloch and others [22][23]. The energy loss by a particle traversing some material, assuming the particle to have charge  $\pm e$ , is described by the Bethe-Block formula:

$$-\frac{dE}{dx} = \frac{Dn_e}{\beta^2} \left[ \ln \left( \frac{2mc^2\beta^2\gamma^2}{I} \right) - \beta^2 - \frac{\delta(\gamma)}{2} \right]$$
 (2.1)

where x is the distance travelled through the medium, m is the electron mass and

$$D = \frac{4\pi\alpha^2\hbar^2}{m} = 5.1 \times 10^{-25} \text{ MeV cm}^{2}.$$
 (2.2)

The other constants are:  $n_e$  for the electron density, I for the mean ionization potential of the atoms averaged over all electrons (given approximately by I=10Z eV for atomic number Z greater than 20),  $\delta(\gamma)$  for a "dielectric screening correction", c is the speed of light (c=299,792,458~m/s),  $\beta$  is v/c (with v being the velocity of the particle),  $\gamma$  is the Lorentz factor, given by  $1/\sqrt{1-\beta^2}$ ,  $\alpha$  is particle charge and  $\hbar$  is  $\hbar/2\pi$ , with  $\hbar$  being the Planck constant ( $\hbar=6.62606957\times10^{-34}~m^2kg/s$ ). The typical behaviour of dE/dx for particles in a detector, according to eq. 2.1, is depicted in fig. 2.1 for protons and pions in lead. This figure shows that different types of particles travelling the same distance range in the same medium lose different amounts of energy, described by eq. 2.1. The range is the total path length for a stopping particle with a given initial energy. Therefore, the range-energy relation can be used for the identification of charged particles [24], and that is the method used in this thesis to develop the FGD particle identification (PID) algorithm.

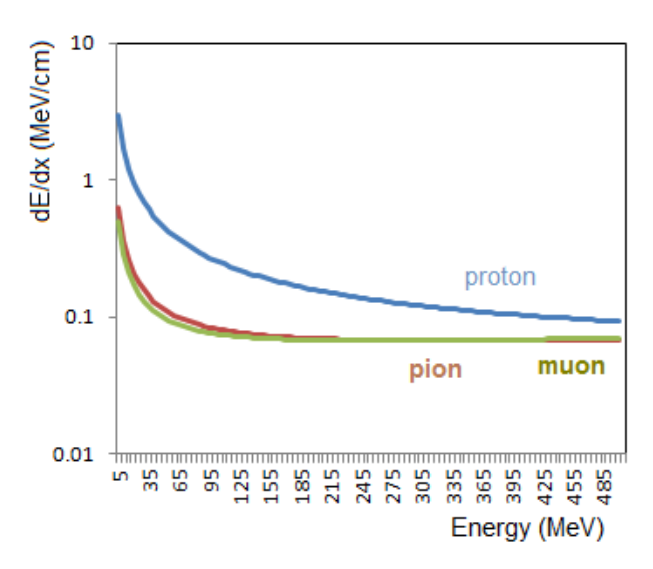


Figure 2.1: Ionization energy loss for charged pions, muons and protons in an organic scintillator. (Original in colour.)

In addition, fig. 2.1 shows that the dE/dx for a given particle depends on its kinetic energy, which can be measured with the FGDs. However, the method used in this thesis will not be based on distributions as depicted in the figure above, but will rather consider the total kinetic energy of the particle left in the FGDs as a function of its total track length (distance travelled). In particular, this work will only use particles fully contained in the FGDs. This will ensure that the total kinetic energy of a given particle is completed deposited in the FGDs, and that the track length associated to this particle corresponds to that total kinetic energy, allowing then a direct comparison between the different properties of different particle species. For example, based on fig. 2.1, for a proton and a pion, the kinetic energy deposited per unit of track length will yield different total distance travelled. Therefore, dividing the total kinetic energy deposited by the proton by its total distance travelled will give a different result from that calculated for the pion, thus providing a parameter to identify between these two particles. This is the

reason why the algorithm described in later sections can only be applied for stopping particles in the FGDs. Particles starting outside the detectors can be seen as particular cases of particles which start in the FGDs, with the difference being that the entry energies in the FGD of those particles can be considered as their initial energies for the sake of the FGD PID algorithm. An extension of the algorithm to particles exiting the FGDs would require the use of information from other detectors, which is beyond the scope of this work.

#### 2.2 Scintillator detectors

The T2K Fine Grained Detectors, as discussed in section 1.3, are based on scintillating bars to detect particles [18]. In this kind of detector, charged particles passing through the scintillating material excite its atoms. When de-excited, these atoms emit light in the ultraviolet (UV) region of the spectrum [3]. The scintillation process is especially evident in organic substances which contain aromatic rings, such as polystyrene (PS) and polyvinyltoluene (PVT) [25].

In the FGDs, the scintillating bars are made of polystyrene doped with PPO (2,5-Diphenyloxazole) and POPOP (1,4-bis(5-phenyloxazol-2-yl) benzene), both organic scintillating materials. The bars are coated with reflective polystyrene doped with TiO<sub>2</sub> [18]. Organic materials, in general, emit light in the ultraviolet range, which is quickly attenuated due to self-absorption effect in the detector material. To mitigate this effect, wavelength shifting (WLS) fibres are used to collect and transport the photons from the point of interaction of the particles in the FGDs to the MPPCs [3]. The WLS fibres used

in the FGDs shift upwards the wavelengths of these photons to the green region of the spectrum to better match the region of maximum peak sensitivity of the MPPCs.

Scintillating materials, however, do not have exactly the same dE/dx behaviour as that described in the previous section because they respond differently to the ionization process than lead, for example. In other words, if the ionization columns resulting from the particle interactions with the detector are very dense, they will emit less light than that expected using eq. 2.1. A semi-empirical correction proposed by J. B. Birks [26] is used to attend to this effect. The Birk's correction is given by:

$$\frac{d\mathcal{L}}{dx} = \mathcal{L}_0 \frac{dE/dx}{1 + k_B dE/dx} \tag{2.3}$$

where  $\mathcal{L}$  is the measured luminescence of the scintillator,  $\mathcal{L}_0$  is the luminescence at low specific ionization density and  $k_B$  is the Birks' constant for a specific scintillator material which is determined by measurement [25].

# **CHAPTER THREE: Methodology**

# 3.1 PDFs development

The Probability Density Functions (PDF) for each detected particle type (electron, muon, pion and proton) in the FGD were developed based on the energy deposition distribution relative to the distance travelled by a given particle (hereafter referred to as track length) in the detector. Since this distribution is characteristic for each different particle type, it can be used to identify between different particle species.

In the FGDs, the energy deposited is obtained by measuring the charge output from each MPPC. Only MPPCs with charge signal above a defined threshold are considered. The threshold was chosen because its value is far below the single-pixel pulse height distribution, but is large enough to avoid most baseline fluctuations. The output charge is then converted to energy using an appropriate conversion factor following the detector calibration. Corrections are then applied to adjust for factors such as light attenuation in the WLS fibers [16]. The resulting charge from each MPPC is summed up to obtain the total energy deposited by a given particle in the detector. This value, however, does not take into account the energy deposited by the particle in dead (non-readout) material between scintillator bars.

The track length is obtained using the RecPack package in the ND280 software [27]. This is an algorithm that reconstructs the path of particle using measured hits (one hit represents a reconstructed point in a scintillator bar with a MPPC signal). RecPack takes into account curvatures in the path produced by the magnets surrounding the detector.

For a given particle species, the respective PDF was obtained using simulations of that particle passing through the detectors. The particle gun option available in the simulation toolkit Geant4<sup>1</sup> (see [28]) was used with the ND280 software package to individually generate samples of protons (p), muons ( $\mu$ ), electrons (e) and pions ( $\pi$ ) with the kinematics of interest to T2K. The ND280 was implemented in the Geant simulation to ensure consistency with the response of the detector. The particles generated had energy uniformly distributed between 0 and 500 MeV. They were also produced at positions uniformly distributed in the detector fiducial volume (active volume within the detector, excluding an external layer) of the detectors FGD1 and FGD2 (fig. 3.1).

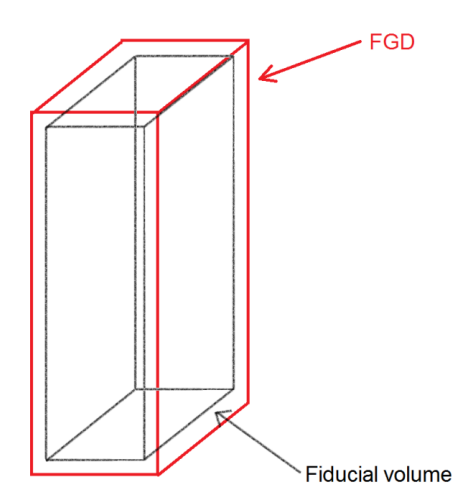


Figure 3.1: Representation of fiducial volume region relative to FGD. (Original in colour.)

100,000 particles of each species were generated with uniform angular distribution in each of the 10-degree (polar) bin size between 0 and  $90^{\circ}$  relative to the beam direction (hereafter referred to as z-direction, as depicted in fig. 3.2), for an overall

<sup>&</sup>lt;sup>1</sup> More information about the toolkit is available at http://geant4.web.cern.ch/geant4/

total of 900,000 particles of each species. A 2-dimensional representation of the angular bins can be seen in fig. 3.3. The idea behind using this method is to ensure enough statistics for each angular interval.

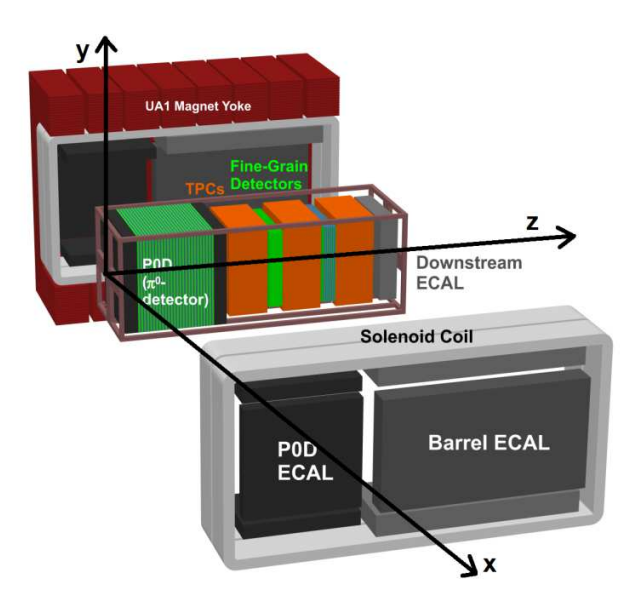


Figure 3.2: Representation of the coordinate axes relative to the neutrino beam direction in the ND280 detector. (Original in colour)

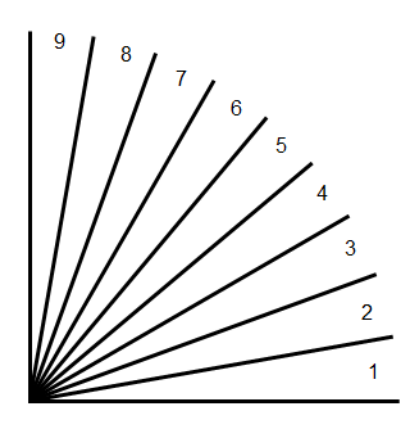


Figure 3.3: 2-dimensional representation of the angular bins used in the simulations.

Not all simulated particles were reconstructed, though. This was due to the efficiency of the reconstruction software package ND280 fgdRecon, that can be affected,

for example, for the number of hits the particle has in the detector (the more hits, the better the reconstruction) [24]. Out of 900,000 generated particles of each species, only the amounts shown in table 3.1 (for FGD1) and table 3.2 (for FGD2) could be reconstructed and, therefore, used in the next step of the analysis.

Particle	Number of reconstructed events	Number of fully contained events
Proton	333,598	79,290
Muon	292,644	45,411
Electron	504,784	20,359
Pion	393,425	2,220

Table 3.1: Number of particles used in generation of the PDFs for FGD1.

Particle	Number of reconstructed events	Number of fully contained events
Proton	196,427	37,107
Muon	220,707	20,506
Electron	348,250	11,649
Pion	246,658	1,217

Table 3.2: Number of particles used in generation of the PDFs for FGD2.

Since the amount of energy deposited per unit distance depends on the momentum of the particle (high momentum particles deposit less energy than low momentum ones), and the FGDs do not provide momentum measurements, it is important to set a standard for comparison when generating the PDFs. For that, only particles starting and stopping within one of the FGDs are used to develop the PDFs. In this way, it is guaranteed that all the energy of a particle was deposited in the detector along its track length. The size of the sample is given by the fraction of reconstructed tracks for which the start and end

points are within the respective FGD fiducial volume (fully contained events). This number can also be seen in table 3.1 and 3.2 (third column to the right). Once these tracks are selected, one can plot the correspondence between the deposited energy and track length.

## 3.2 Energy and track length

The obtained plots using the simulations described in section 3.1 are shown in fig. 3.4 to 3.7, for protons, muons, electrons and pions in FGD1, respectively (results for FGD2 were omitted for being similar to those obtained for FGD1). All plots on the left-hand side represent the true values of the simulated particle energy and track length. The plots on the right-hand side show the same variables, but with values obtained from the reconstruction software (therefore subjected to smearing effects such as those introduced due to detector resolution).

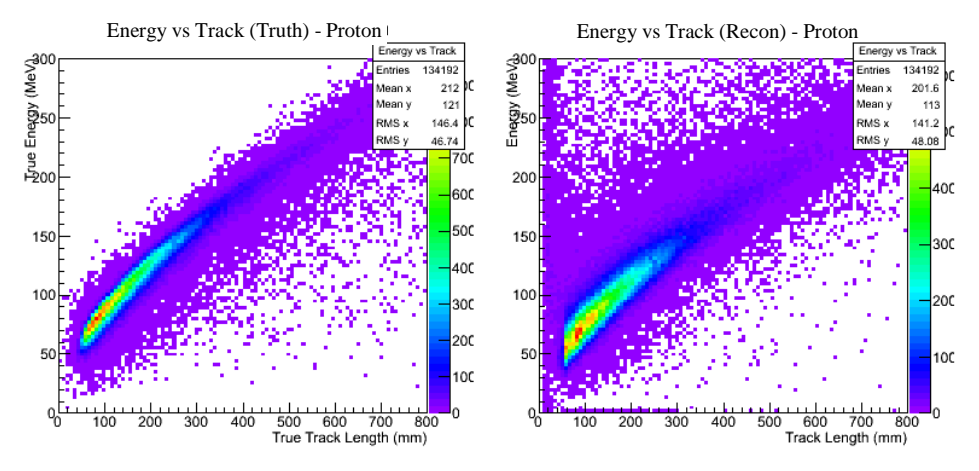


Figure 3.4: Correlation between energy and track length for protons in FGD1 using truth (left-hand side) and reconstructed (right-hand side) variables. (Original in colour.)

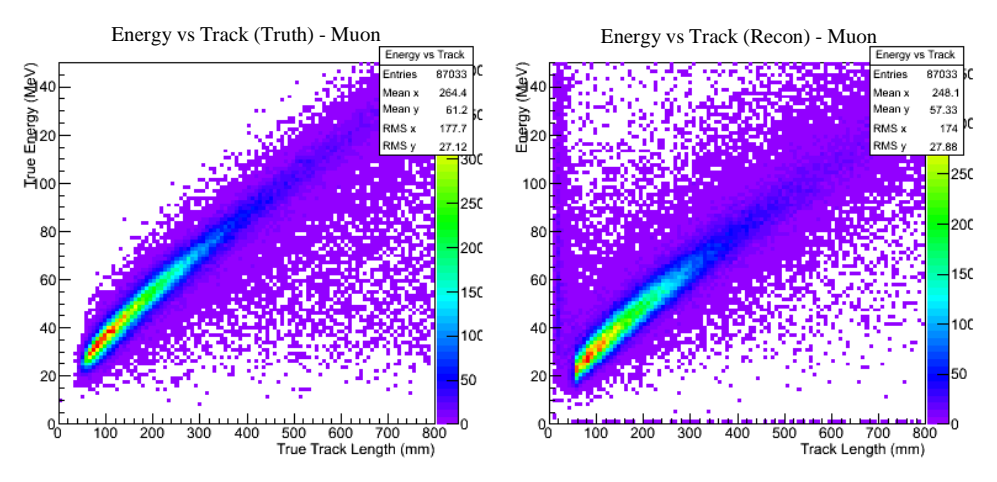


Figure 3.5: Correlation between energy and track length for muons in FGD1 using truth (left-hand side) and reconstructed (right-hand side) variables. (Original in colour.)

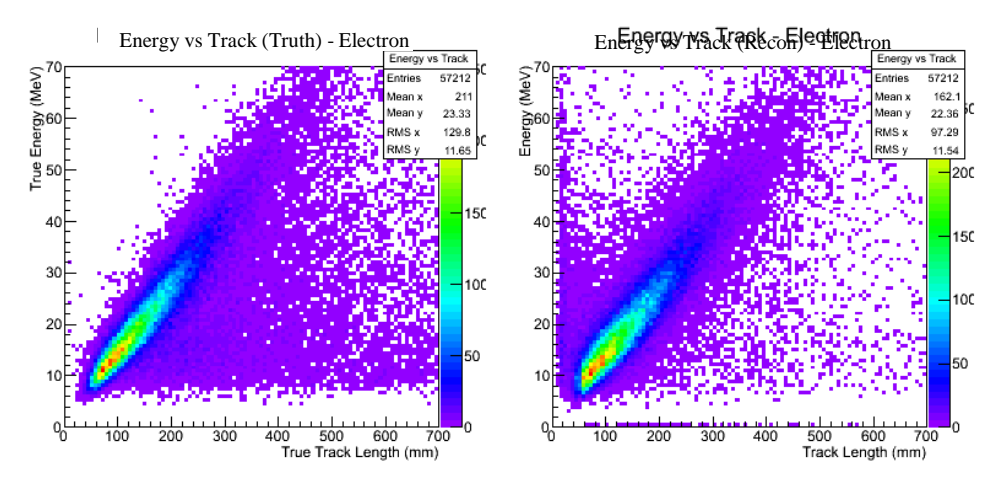


Figure 3.6: Correlation between energy and track length for electrons in FGD1 using truth (left-hand side) and reconstructed (right-hand side) variables. (Original in colour.)

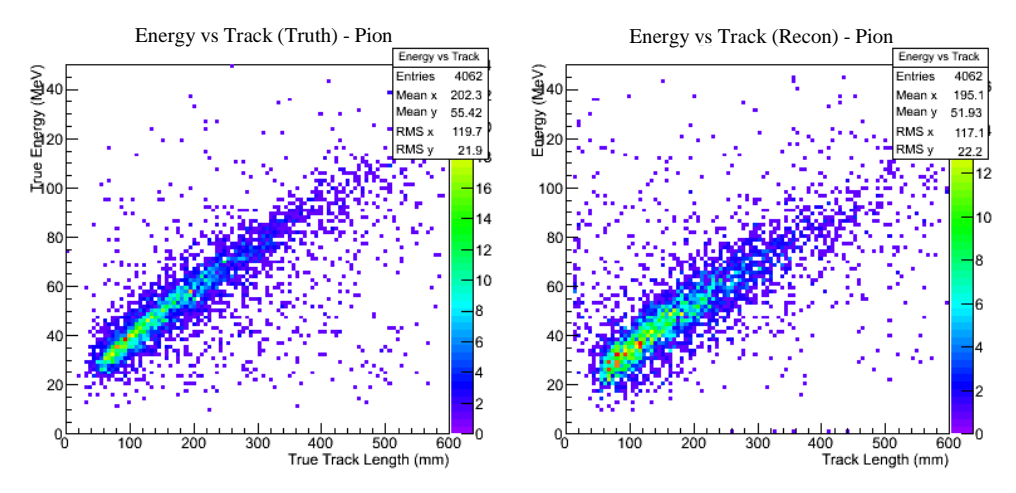


Figure 3.7: Correlation between energy and track length for pions in FGD1 using truth (left-hand side) and reconstructed (right-hand side) variables. (Original in colour.)

The plots made with true information show a very broad distribution of particles around the line where most of the other particles' energy and track length relationship fall. They correspond to events with angle higher than 70° relative to z-direction. This happens because the method used in the reconstruction algorithm gets worse as the angles approach 90°. Removing the tracks with angles above 70° makes the *track length vs energy* distributions agree better between true and reconstructed as can be seen in figs. 3.8-3.11 for FGD1 and in figs. 3.12-3.15 for FGD2, for protons, muons, electrons and pions, respectively. Rare cases of tracks with problems in the reconstruction such as negative track lengths or negative energies were also neglected without any consequence in the building of the PDFs.

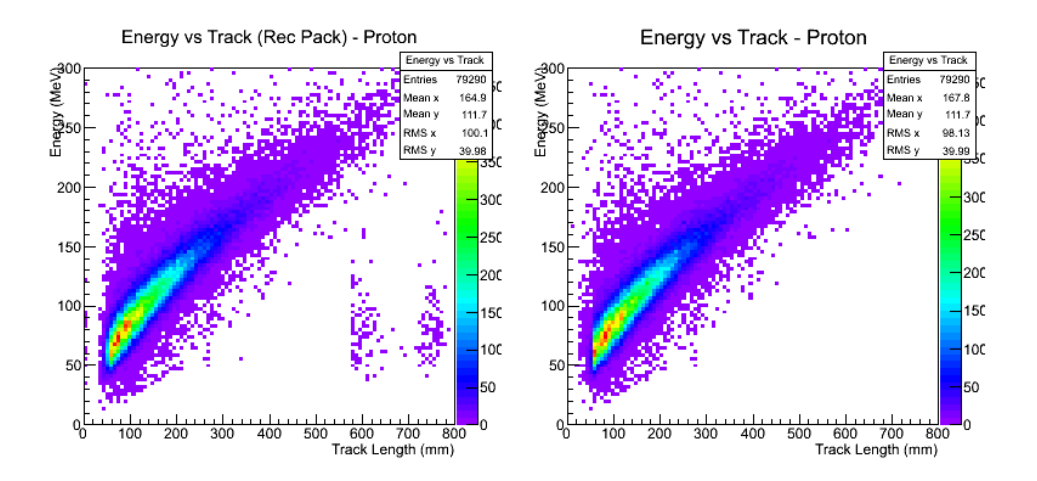


Figure 3.8: Correlation between energy and track length for protons in FGD1 with angles smaller than 70°. (Original in colour.)

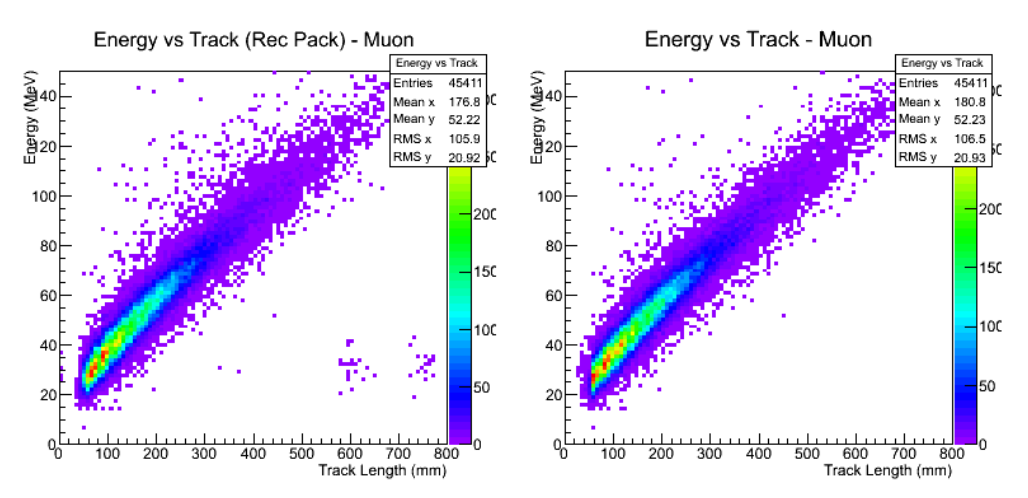


Figure 3.9: Correlation between energy and track length for muons in FGD1 with angles smaller than  $70^{\circ}$ . (Original in colour.)

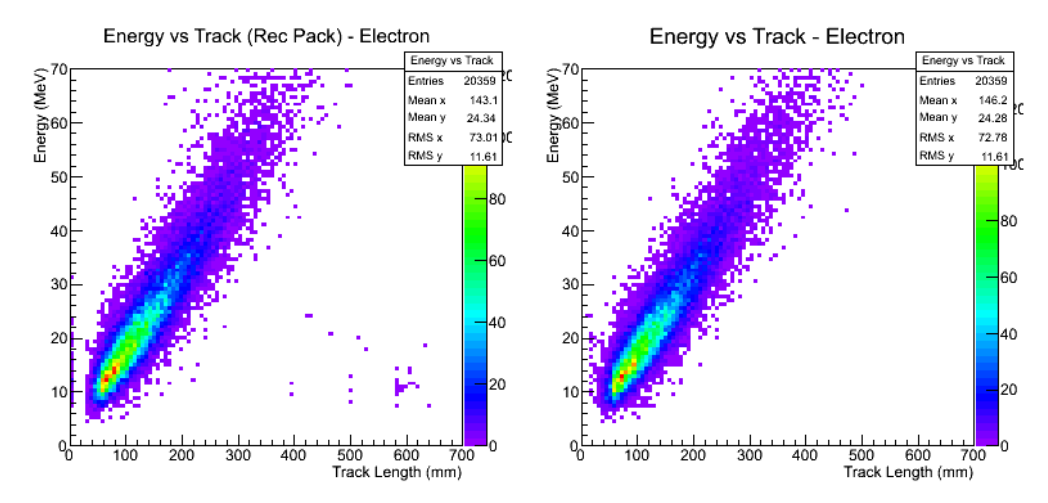


Figure 3.10: Correlation between energy and track length for electrons in FGD1 with angles smaller than 70°. (Original in colour.)

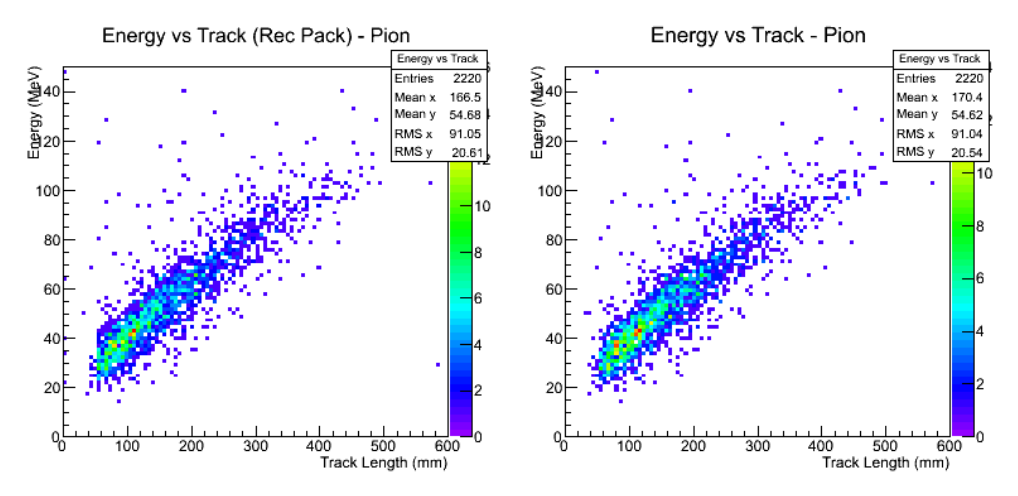


Figure 3.11: Correlation between energy and track length for pions in FGD1 with angles smaller than 70°. (Original in colour.)

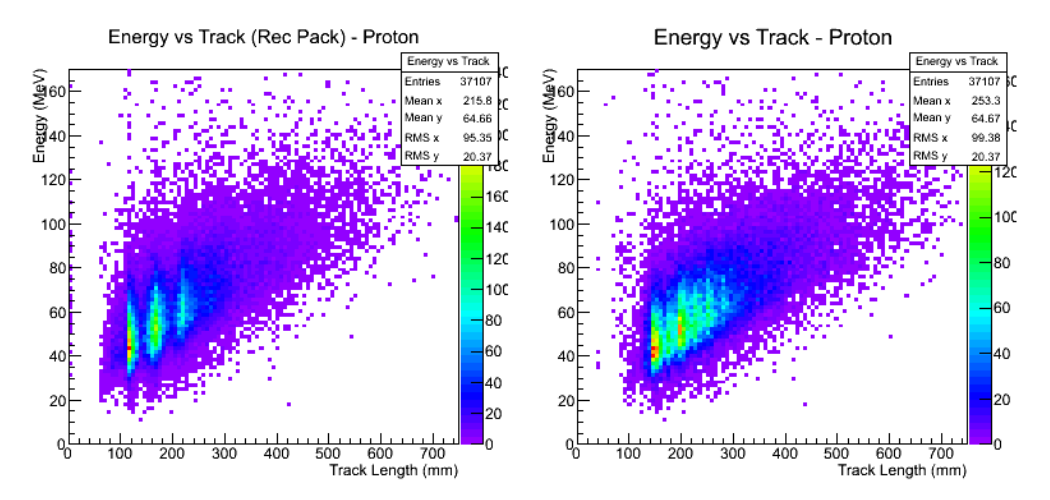


Figure 3.12: Correlation between energy and track length for protons in FGD2 with angles smaller than 70°. (Original in colour.)

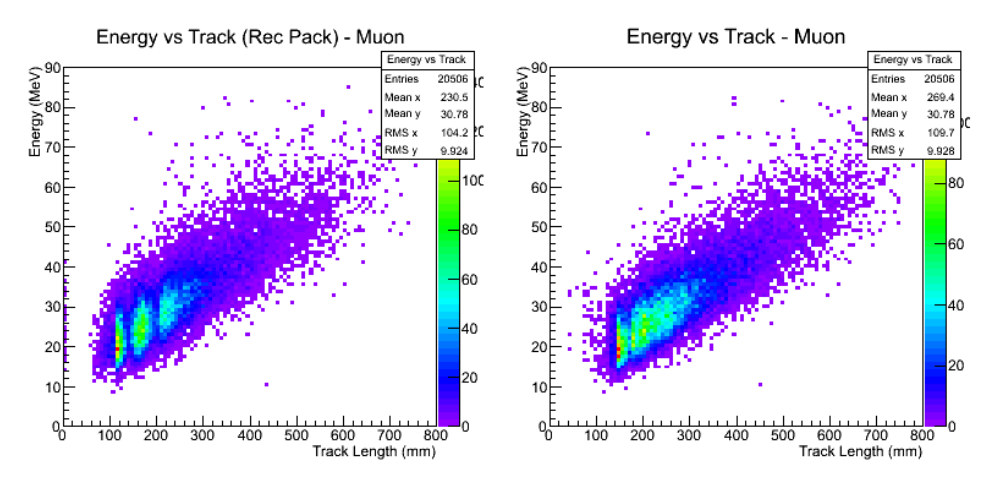


Figure 3.13: Correlation between energy and track length for muons in FGD2 with angles smaller than 70°. (Original in colour.)

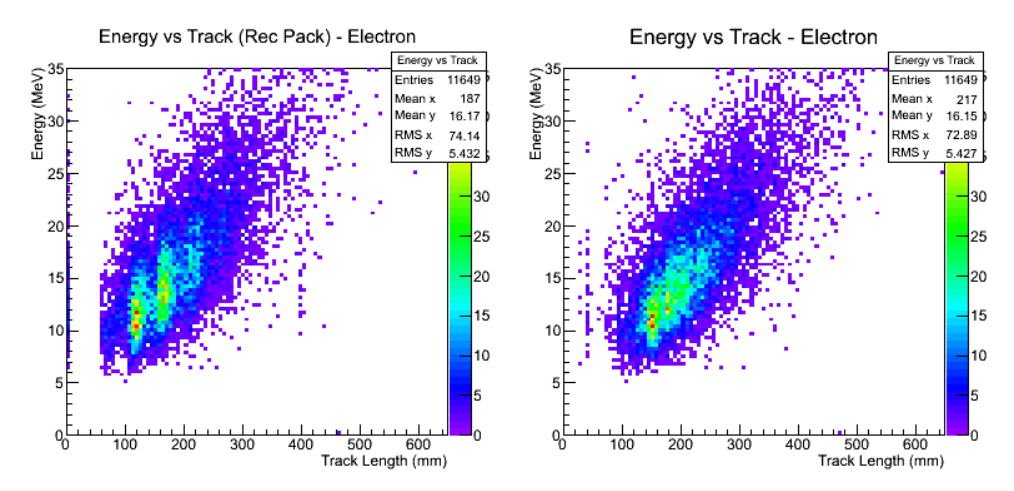


Figure 3.14: Correlation between energy and track length for electrons in FGD2 with angles smaller than 70°. (Original in colour.)

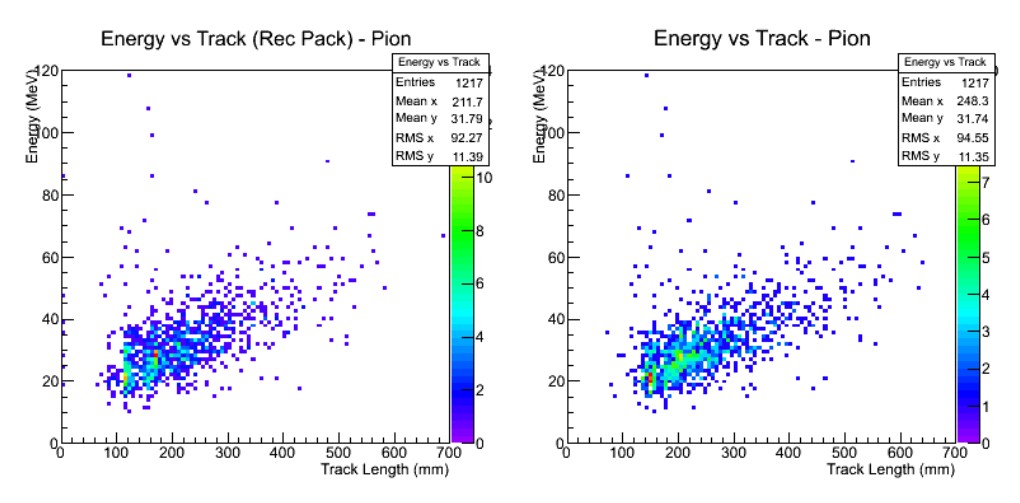


Figure 3.15: Correlation between energy and track length for pions in FGD2 with angles smaller than 70°. (Original in colour)

The plots for FGD2 show a clear structure in the track length, where one can clearly see a pattern of what looks like vertical lines with higher concentration of events. This is explained by the larger distances between active layers in FGD2 compared to FGD1. The reason is that the water layers in FGD2 are not active (do not have a readout system). Therefore, if a particle starts or stops in a water layer, the hit used to reconstruct the track is located either in the bar immediately after or before that layer, respectively.

A more detailed study of these particle samples is done by individually analysing the distributions for many parameters, such as energy deposited, track length and angle, in each detector, and by comparing the respective true and reconstructed information to assess how well those variables are reconstructed.

The distributions of energy are depicted in fig. 3.16 for FGD1 and in fig. 3.17 for FGD2, with red and dashed black lines representing true and reconstructed energies, respectively.

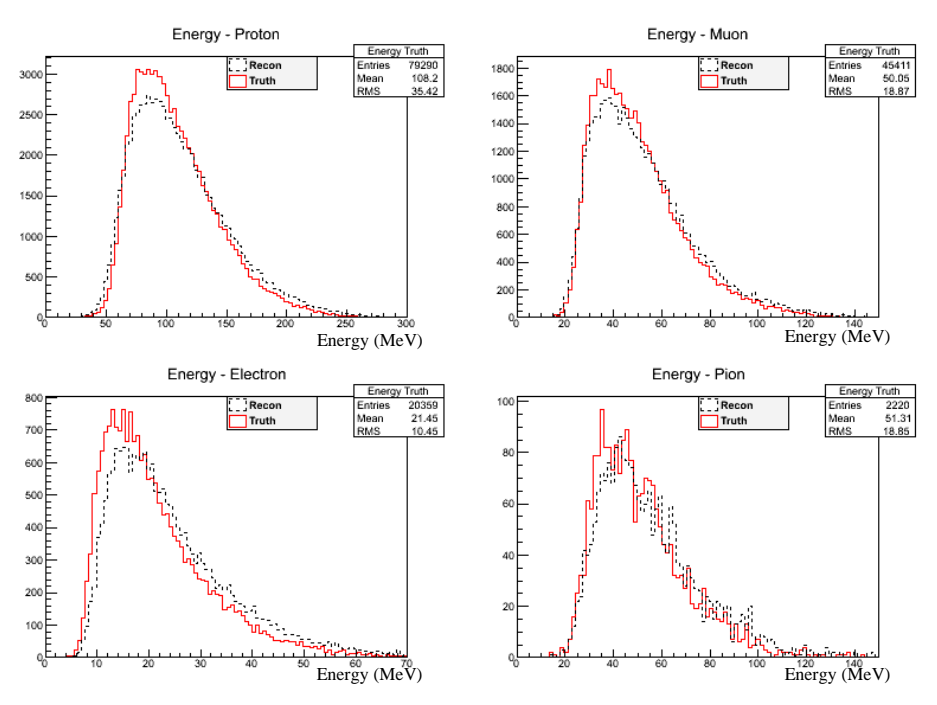


Figure 3.16: Energy distribution for protons (top left), muons (top right), electrons (bottom left) and pions (bottom right) in FGD1. Full red lines are true energy. Dashed black lines are reconstructed energies. (Original in colour.)

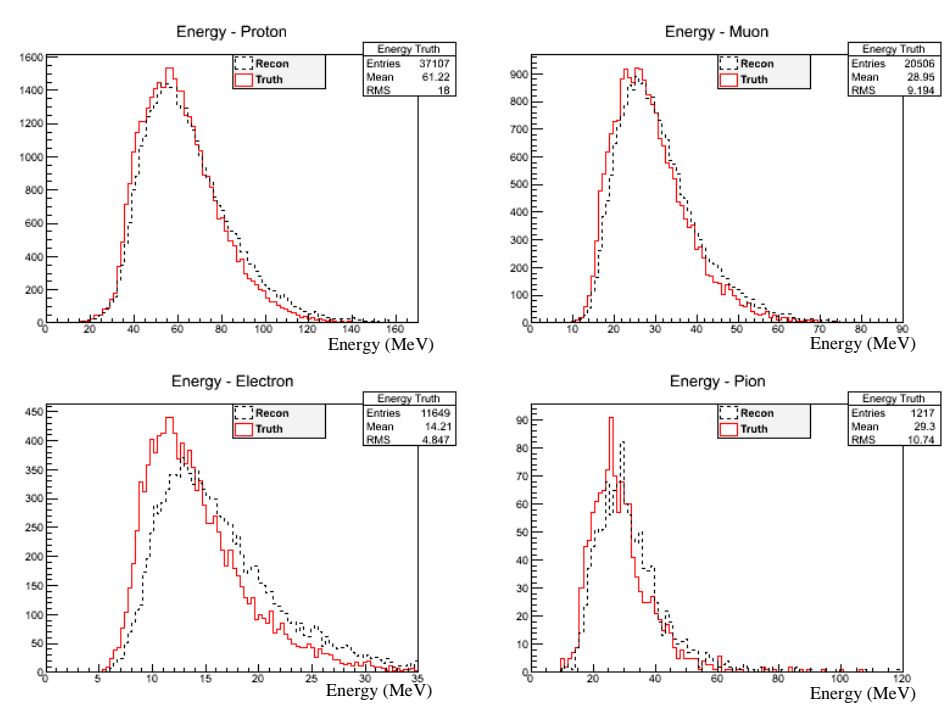


Figure 3.17: Energy distribution for protons (top left), muons (top right), electrons (bottom left) and pions (bottom right) in FGD2. Full red lines are true energy. Dashed black lines are reconstructed energies. (Original in colour.)

The reconstructed energies are shifted relative to the true distributions, as observed in the above figures. The results of the subtraction between the true and reconstructed energies shown above are represented in fig. 3.18 for FGD1. The mean of the distributions are 2.927 MeV for protons, 2.195 MeV for muons, 3.491 MeV for pions and 3.045 MeV for electrons.

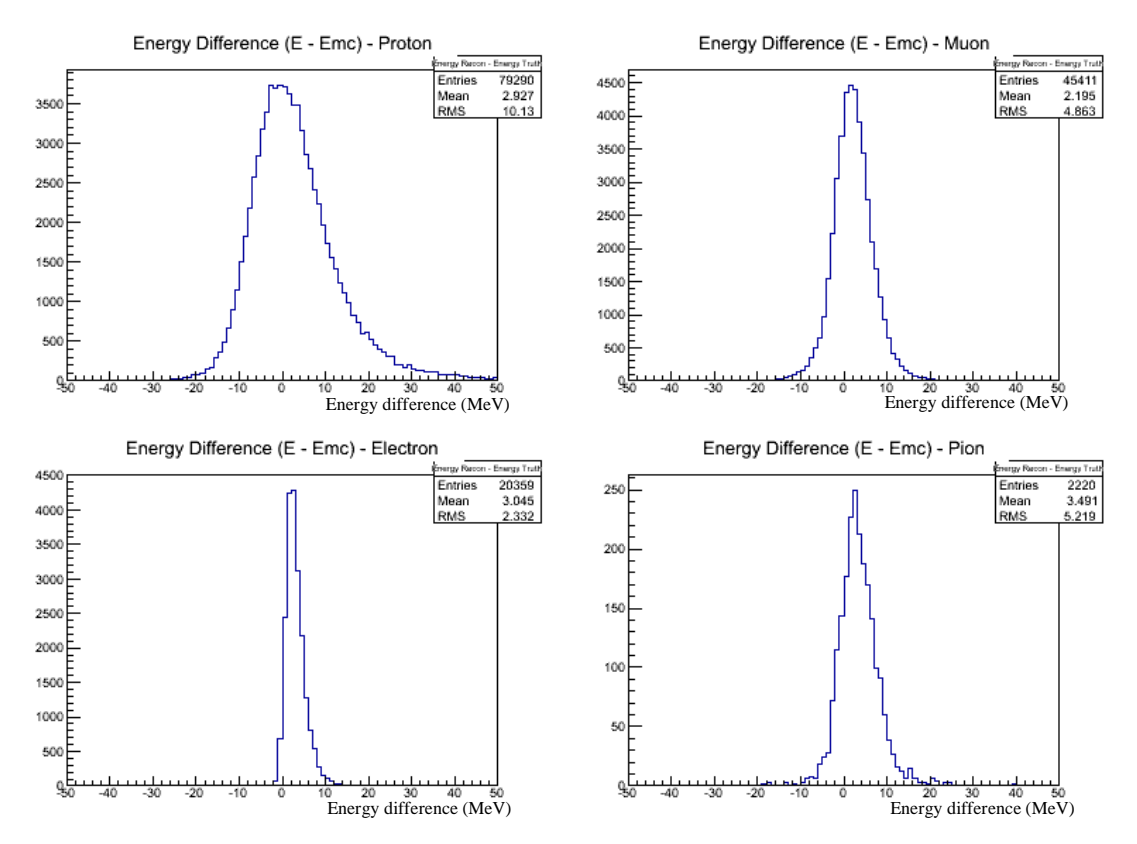


Figure 3.18: Difference in energy between reconstructed and true energy for simulated protons (top left), muons (top right), electrons (bottom left) and pions (bottom right) in FGD1. (Original in colour.).

The distributions for track length are found in fig. 3.19 for FGD1 and fig. 3.20 for FGD2, with red and dashed black lines representing true and reconstructed track lengths, respectively. Each track length is obtained using the reconstruction software package RecPack<sup>2</sup>, which applies the Kalman Filter<sup>3</sup> algorithm [29] with a smoothing method for fitting the hits used to reconstruct the track. This method takes into account the curvatures in the particle trajectory due to the presence of a magnetic field in the detector.

\_

is updated using a weighted average as new measurements are input. In the end, it uses the estimate with the lower level of uncertainty found.

<sup>&</sup>lt;sup>2</sup> RecPack is an external reconstruction toolkit. More information can be found at: http://ific.uv.es/recpack;
<sup>3</sup> Kalman Filter is a recursive algorithm based in a series of measurements (each with its level of uncertainty). For each measurement, the algorithm generates an estimate of the unknown parameters, which

The true track is obtained by fitting a straight line between the initial and final hit positions. The straight line is a good approximation in the case of these particle trajectories, because, since only stopping particles are being analyzed, the energies involved are very low and, consequently, the curvature caused by the magnet is also low.

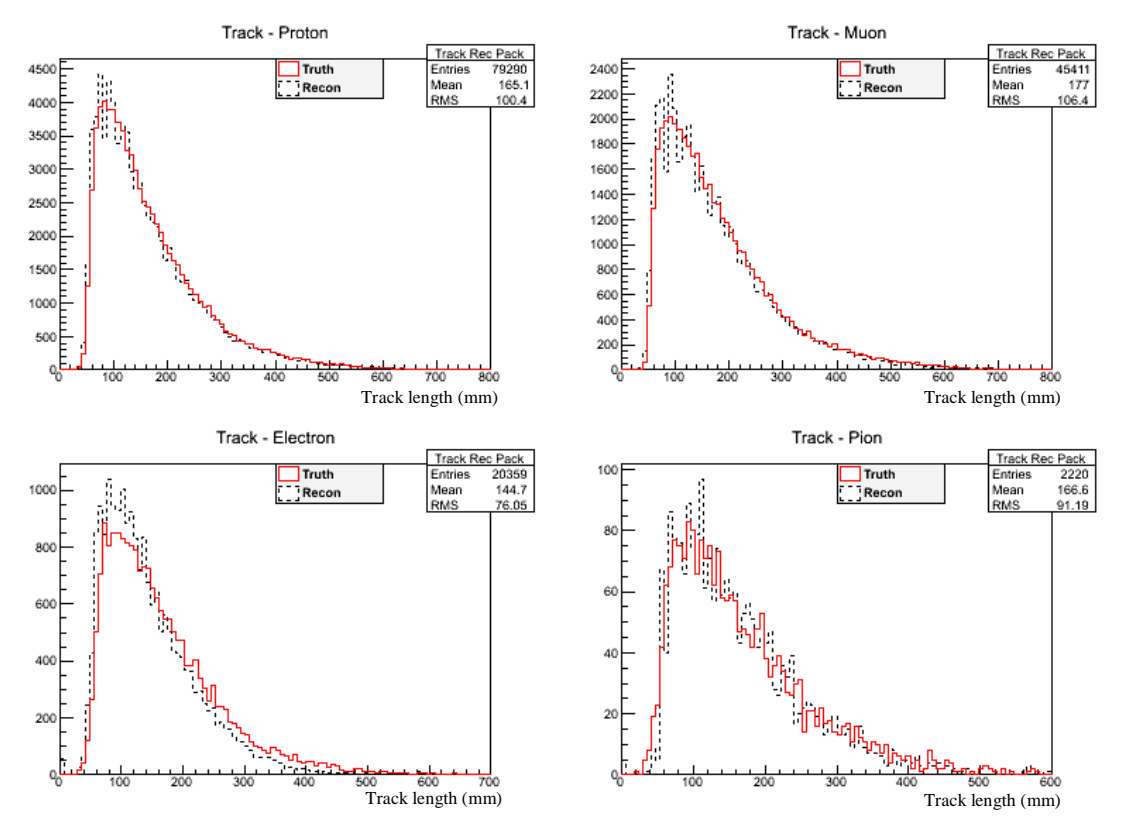


Figure 3.19: Track length distribution for protons (top left), muons (top right), electrons (bottom left) and pions (bottom right) in FGD1. Full red lines are true track lengths.

Dashed black lines are reconstructed track lengths. (Original in colour.)

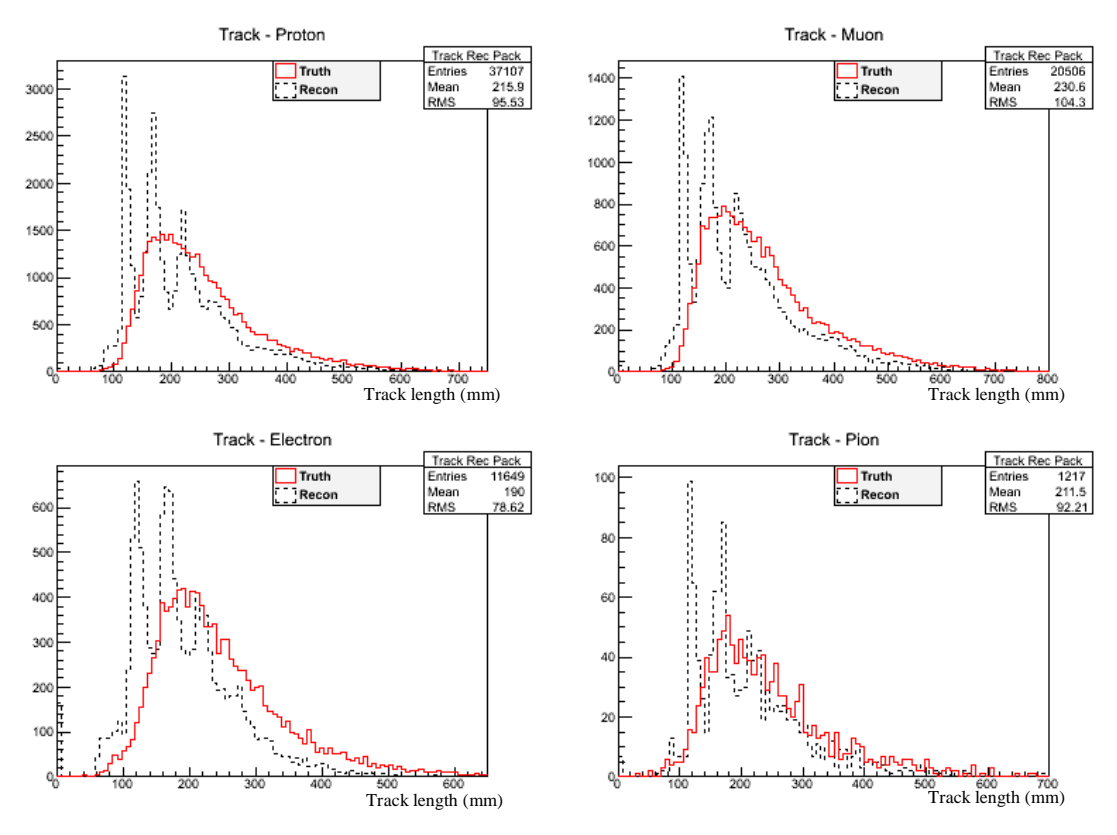


Fig. 3.20: Track length distribution for protons (top left), muons (top right), electrons (bottom left) and pions (bottom right) in FGD2. Full red lines are true track lengths.

Dashed black lines are reconstructed track lengths. (Original in colour.)

The track length distributions clearly agree better between the true and reconstructed values than those observed for the energies in FGD1. The larger differences between true and reconstructed values and the structures observed in the reconstructed track lengths for FGD2 are due to the presence of the non-readout water layers (25 mm each) as already discussed in section 1.3 (paragraph 4).

### 3.3 Probability density functions

The comparisons between true and reconstructed variables, as discussed in the previous sections, serve to demonstrate that, despite a few differences between these two classes of variables, there are good agreements either in shape or general trend between them. This is fundamental for the selected method used to develop the particle identification algorithm. As it will be described in the following section, only reconstructed quantities (simulated and real data) will play a role in the construction of each particle type probability density function (PDF, which are functions that describe the probability of a variable to acquire a given value). Therefore, any difference between true and reconstructed variable will not play a role in the final particle identification algorithm.

According with the theoretical description [21][24], the energy deposition per unit or track length is characteristic of each particle species (see section 2.1). The PDFs were constructed using the data shown in figs. 3.8 to 3.15 with the track length divided into 10 mm bins. For each of these track length bins, the energy distribution is plotted and then fitted using a Gaussian function (only bins with more than ten entries are considered in order to guarantee a minimum statistic significance). A PDF is then constructed for a given particle species using the mean energy values obtained from each fit. The standard deviations resultant from each fit are also used in the analysis as a way to measure how much, in average, an experimental event deviates from the mean value.

The resulting PDFs for each particle are shown in fig. 3.21 for FGD1 and fig. 3.22 for FGD2. Here, the points represent the mean values coming from the fittings and the error bars represent the standard deviations. Some points were excluded from the plots

due to having very large standard deviations (more than 50 MeV), suggesting that they were bad points, since a very large sigma means that the energies measured for that track length bin varied a lot. Whenever the energy distribution for each bin had less than ten entries, and the Gaussian fit was not performed, the point was also not included in the plot.

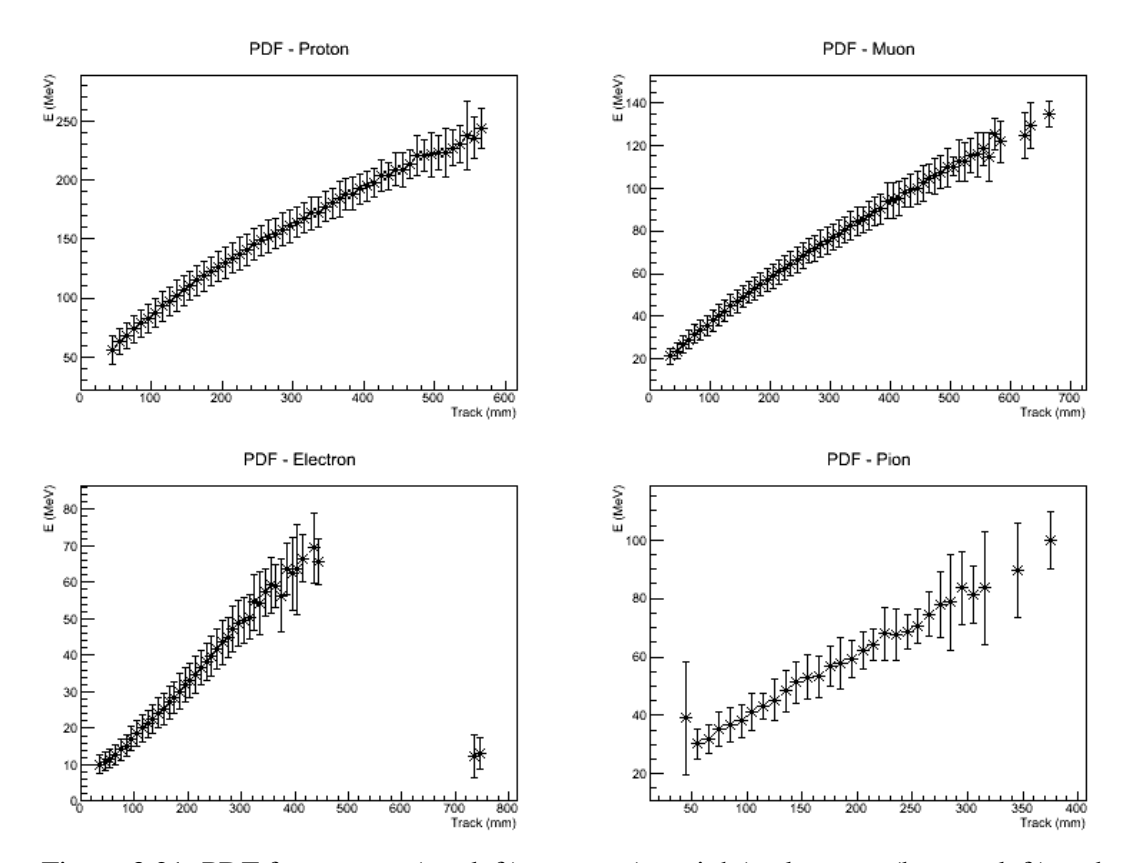


Figure 3.21: PDF for protons (top left), muons (top right), electrons (bottom left) and pions (bottom right) in FGD1.

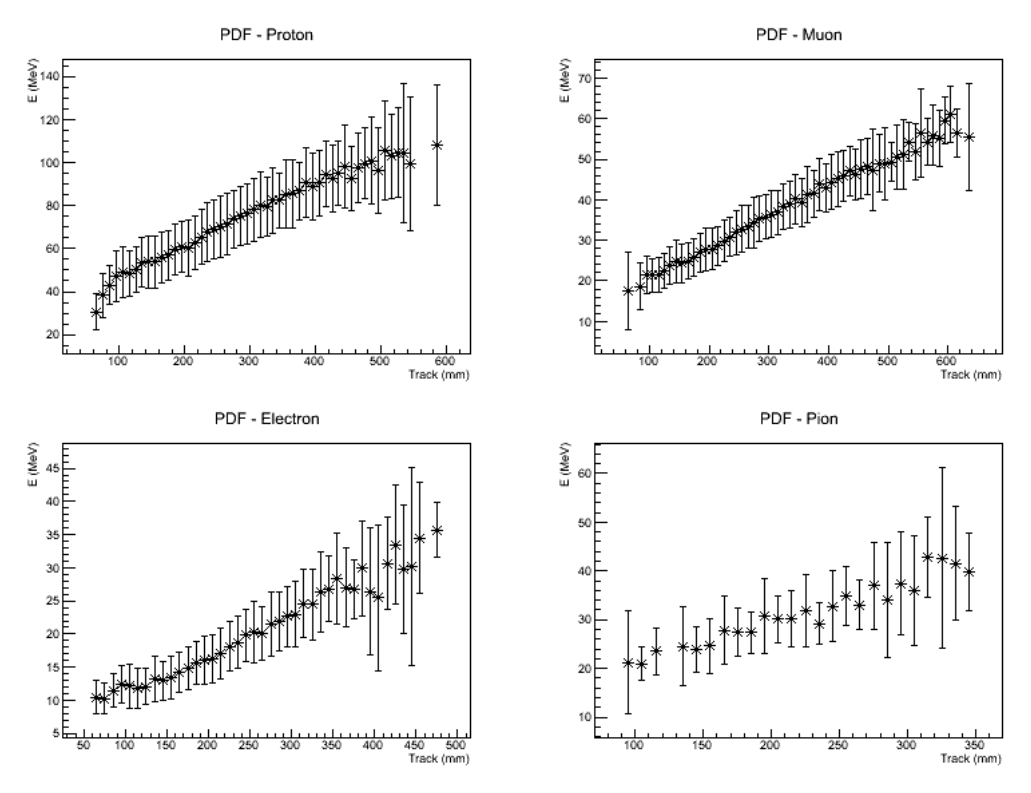


Figure 3.22: PDF for protons (top left), muons (top right), electrons (bottom left) and pions (bottom right) in FGD2.

# 3.4 Likelihood analysis

The track lengths and energies from the real (non-simulated) particles crossing the detector can be compared to the values given by the PDFs (which were calculated based on simulations). The comparison used in this particle identification algorithm is given by the pull, a value derived from how much the energy of a given particle deviates from that based on a calculated PDF for a determined track length and particle hypothesis. The pull for each particle type hypothesis i is given by:

$$pull_i = \frac{E - E_i(x)}{\sigma_i(x)} \tag{3.1}$$

where, i = (proton, electron, muon, pion); E is the energy from the real particle crossing the detector;  $E_i(x)$  is the standard energy from the PDFs corresponding to a given track length x and  $\sigma_i(x)$  is the standard deviation associated to  $E_i(x)$ .

In practice, the real particle is tested for different particle hypotheses. The hypothesis providing the pull closer to zero is assumed to be the identity of that particle. For example, if the muon hypothesis is the one that gives a pull closer to zero compared to other hypothesis, then the particle is assumed to be a muon.

Two complementary ways of calculating the pull variable were developed and implemented in the particle identification algorithm: the first one (from now on referred to as the "table method") assumes the values for the energies and their respective standard deviations as those presented in Figs. 3.21 and 3.22 (the data is shown in a graph in order to facilitate the comprehension); the second one (from now on referred to as "fitting method") assume the energies and standard deviations are plotted against the track lengths. In this method, the *energy vs track length* distributions are fitted using eq. 3.2, while the functional form represented in eq. 3.3 is used to fit the *standard deviation vs track length* distributions.

$$f = ax^b + cx (3.2)$$

$$g = ax + b \tag{3.3}$$

The fittings using eq. 3.2 are shown in Figs. 3.23 and 3.24 for FGD1 and FGD2, respectively, while the fitting using eq. 3.3 are depicted in Figs. 3.25 and 3.26 for FGD1 and FGD2, respectively with the resulting parameters listed in tables 3.3 and 3.5 for eq. 3.2 and FGD1 and tables 3.4 and 3.6 for eq. 3.3 and FGD2. Each set of parameters are used as input in each of the respective equations 3.2 and 3.3 for the pull calculations. If

one wants to calculate the proton pull, for example, the proton in FGD1, fitting parameters are applied to equation 3.2, resulting in

$$f = 5.1x^{0.590} + 0.04x \tag{3.4}$$

then the same is done for the standard deviation and the track length substitutes x to obtain the corresponding pull.

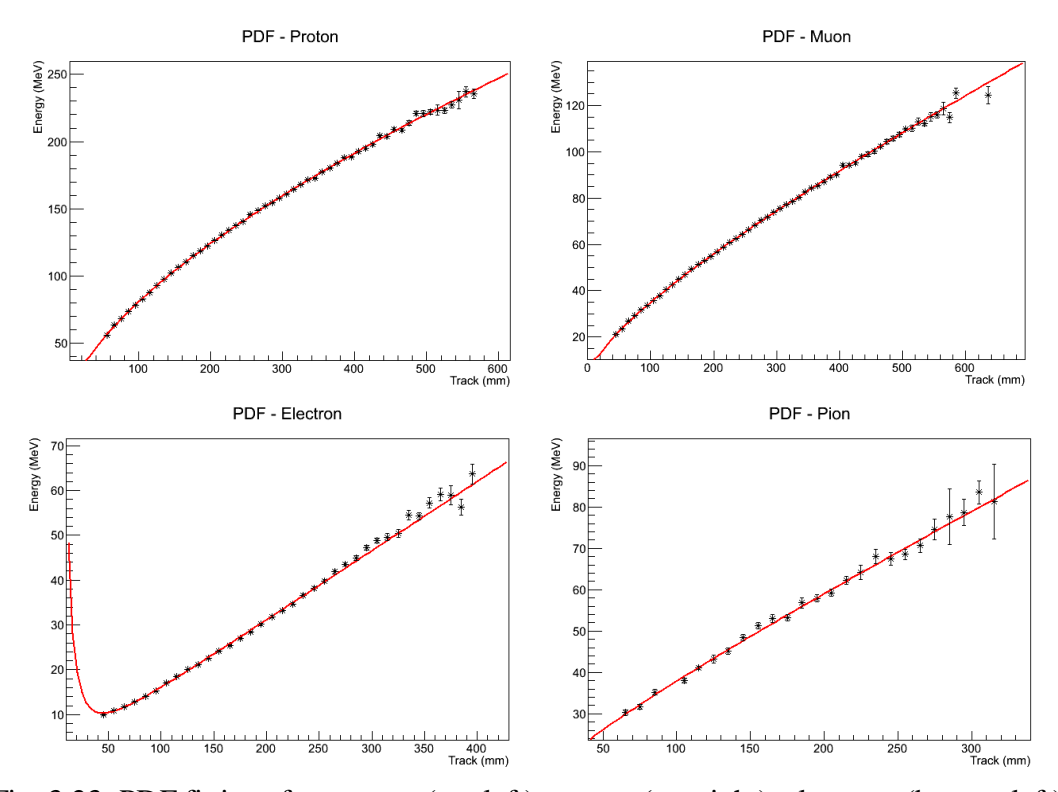


Fig. 3.23: PDF fittings for protons (top left), muons (top right), electrons (bottom left) and pions (bottom right) in FGD1. (Original in colour.)

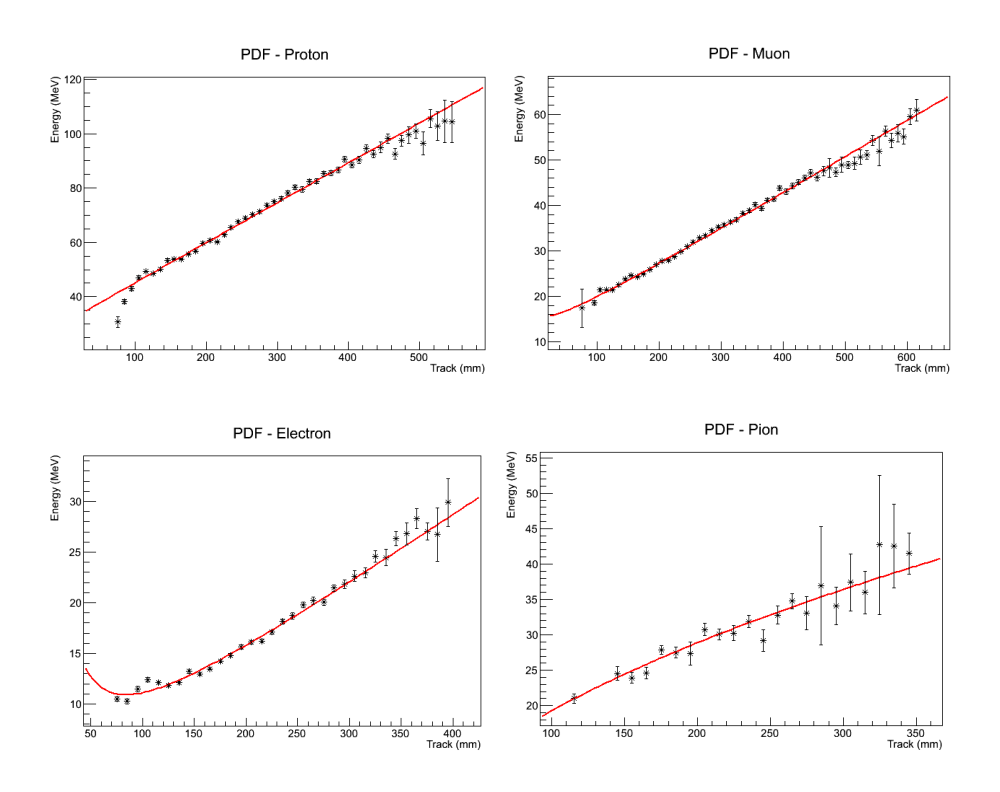


Fig. 3.24: PDF fittings for protons (top left), muons (top right), electrons (bottom left) and pions (bottom right) in FGD2. (Original in colour.)

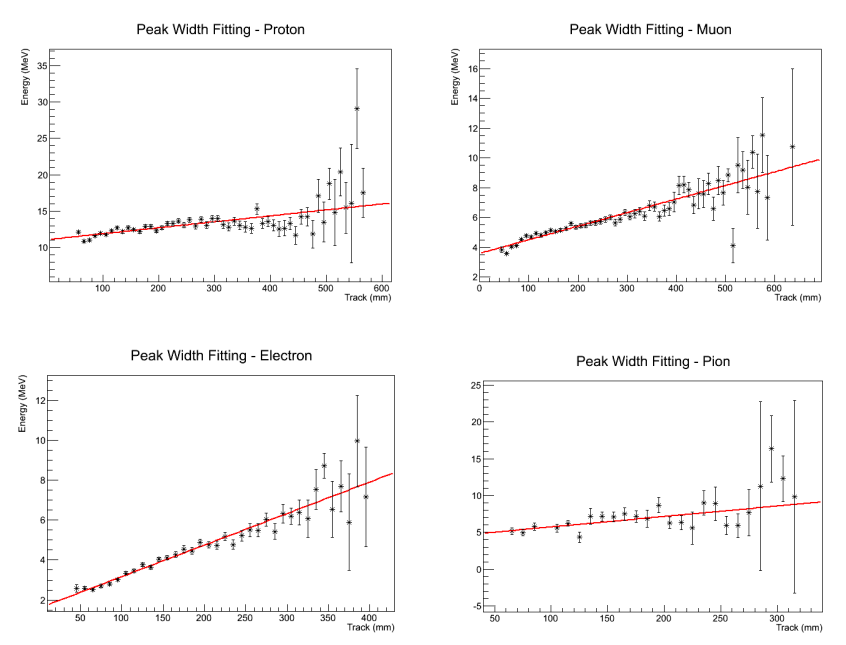


Fig. 3.25: Standard deviation fittings for protons (top left), muons (top right), electrons (bottom left) and pions (bottom right) in FGD1. (Original in colour.)

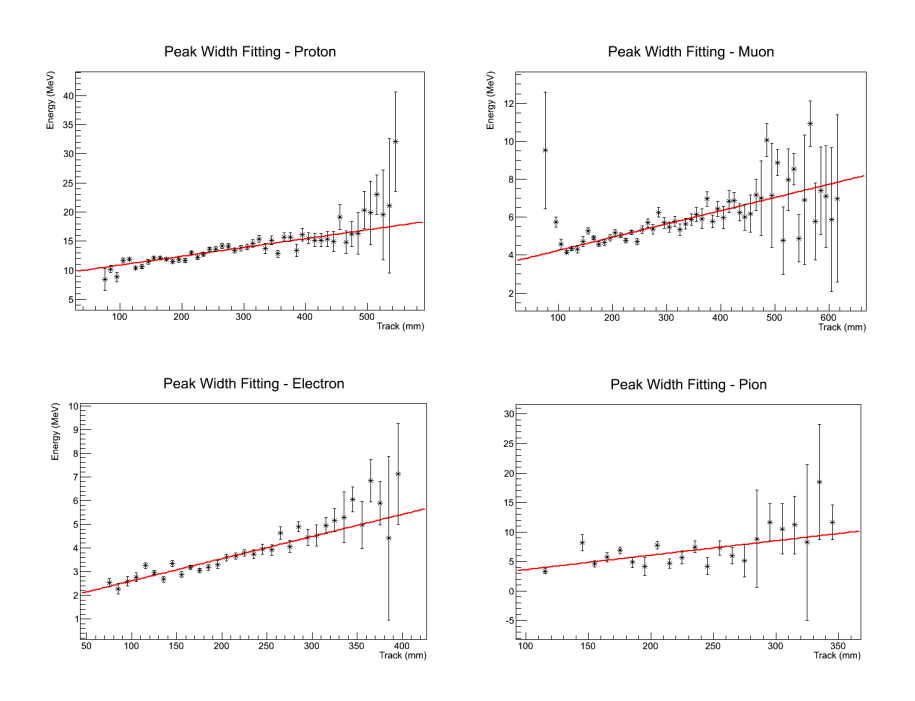


Fig. 3.26: Standard deviation fittings for protons (top left), muons (top right), electrons (bottom left) and pions (bottom right) in FGD2. (Original in colour.)

Particle	Fitting Parameters			
	a	b	С	$\chi^2$ / ndf
Proton	5.1±0.1	0.590±0.009	0.04±0.01	142/49
Muon	2.33±0.09	0.51±0.01	0.105±0.005	126/53
Electron	$(7\pm4)\cdot10^3$	-2.0±0.1	0.1550±0.0004	84/33
Pion	7±4	0.2±0.1	0.18±0.03	19/22

Table 3.3: Fitting parameters using eq. 3.2 for the PDFs in FGD1 (fig. 3.23).

Particle	Fitting Parameters			
	a	b	С	χ²/ ndf
Proton	29±4	0.00±0.03	0.146±0.005	279/45
Muon	19±4	0.10±0.04	0.081±0.002	161/51
Electron	$(8\pm3)\cdot10^2$	-1.15±0.09	0.0697±0.0007	127/30
Pion	1.18±0.09	0.63±0.02	-0.02±0.01	19/19

Table 3.4: Fitting parameters using eq. 3.2 for PDFs in FGD2 (fig. 3.24).

Particle	Fitting Parameters		
1 at tiere	a	b	$\chi^2$ / ndf
Proton	11.07±0.08	0.0082±0.0005	177/50
Muon	3.60±0.04	0.0091±0.0002	172/54
Electron	1.68±0.05	0.0150±0.0004	113/39
Pion	4.3±0.4	0.014±0.003	27/23

Table 3.5: Fitting parameters using eq. 3.3 in standard deviation for FGD1 (Fig. 3.25).

Particle	Fitting Parameters		
1 ar ticic	a	b	$\chi^2$ / ndf
Proton	9.4±0.2	0.0151±0.0008	121/46
Muon	3.55±0.08	0.0070±0.0004	151/52
Electron	1.7±0.1	0.0094±0.0005	72/31
Pion	1.2±0.8	0.024±0.005	39/20

Table 3.6: Fitting parameters using eq. 3.3 in standard deviation for FGD2 (Fig. 3.26).

To build the final particle identification algorithm, the pull is obtained using the table method for all data points present in the PDFs. The fitting method is employed

whenever the table method does not provide a point for the specific track length being analysed.

The pull distribution for each hypothesis, as given by eq. 3.1, is fitted with a Gaussian function. The likelihood of a given particle hypothesis is given as the ratio between the weight obtained from the Gaussian fit (fitting using a Gaussian function) to this particular hypothesis and the sum of the weights of all other Gaussian fits for all particle hypotheses as mathematically describe in eq. 3.5:

$$W = \frac{Gaus_i(pull_i)}{\sum_j Gaus_j(pull_i)}$$
 (3.5)

where i, j = 1, ..., 4 are the possible particle hyphotesis.

The most suitable hypothesis for a sample should have weight close to one when the pull is close to zero. The results obtained for the pull distribution and weight can be found in section 4.1 for simulations and 4.2 for real data from the experiment.

### **CHAPTER FOUR: Results**

#### 4.1 Pull results

In order to obtain the pull results and test the PDFs obtained, a new set of simulations was developed using the particle gun option in the GEANT simulation package. The same parameters, but different generator seeds were used in order to obtain a different set of data from those used for the construction of the PDFs (see section 3.1 for the discussion on the simulation procedure).

The truth identity of each generated particle was stored throughout the entire simulation so that the efficiency of the particle identification (PID) algorithm could be tested, i.e., how many times a given particle species is identified as the true identity of generated particles after all the simulation and data reconstruction processes are considered. Therefore, for each type of sample (proton, muon, electron or pion), all four-particle hypotheses were used to obtain the respective pull values. The pull distributions for FGD1 are shown in figs. 4.1 to 4.4 and, for FGD2, in figs. 4.5 to 4.8. All figures on the left-hand side were obtained using obtain the table method, while the ones located on the right-hand side were obtained using the fitting method.

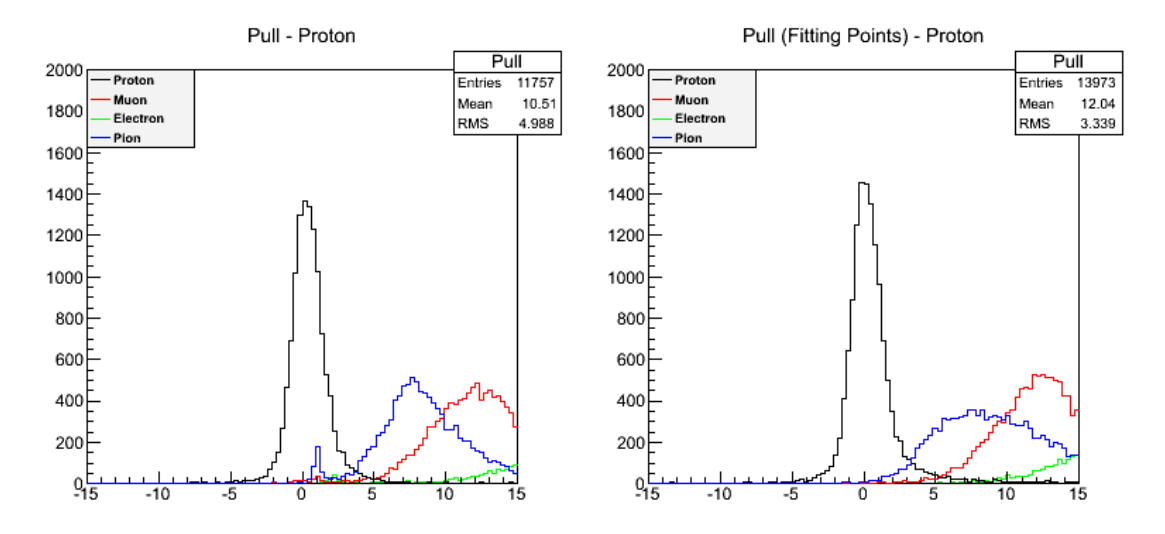


Figure 4.1: Pull distributions for each particle hypothesis assuming a pure proton sample in FGD1. (Original in colour.)

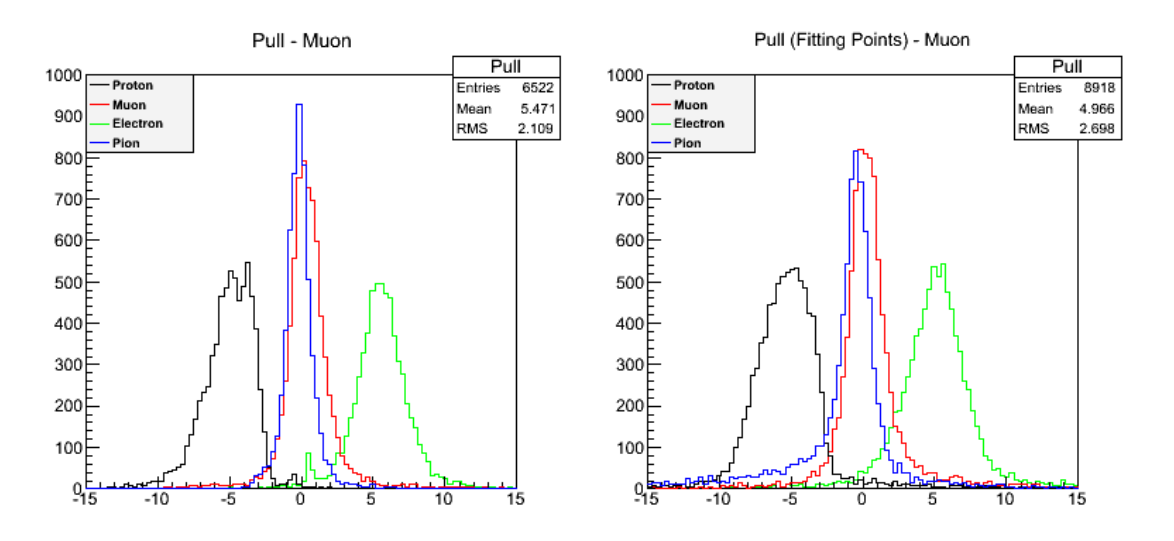


Figure 4.2: Pull distributions for each particle hypothesis assuming a pure muon sample in FGD1. (Original in colour.)

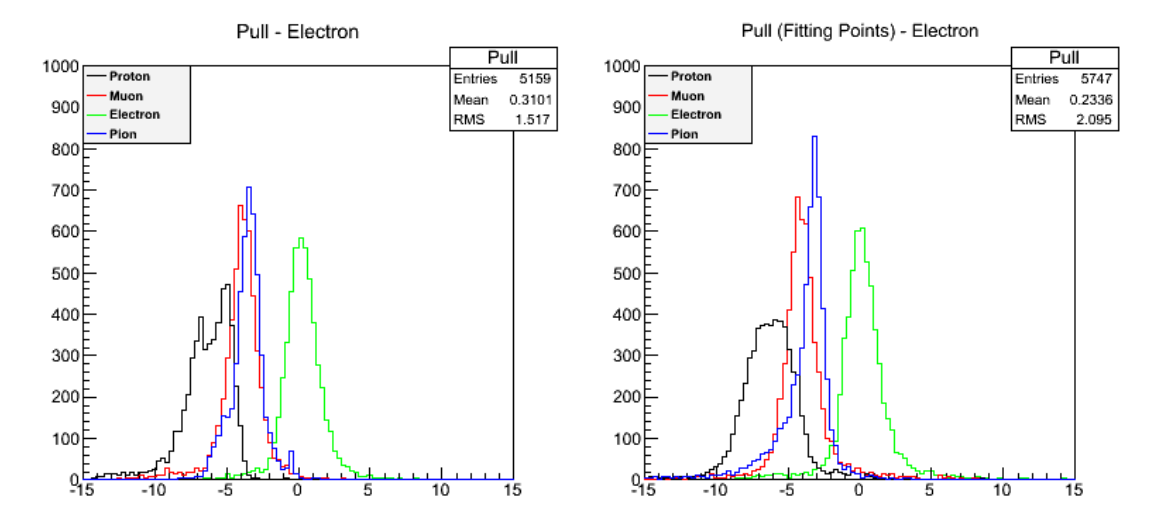


Figure 4.3: Pull distributions for each particle hypothesis assuming a pure electron sample in FGD1. (Original in colour.)

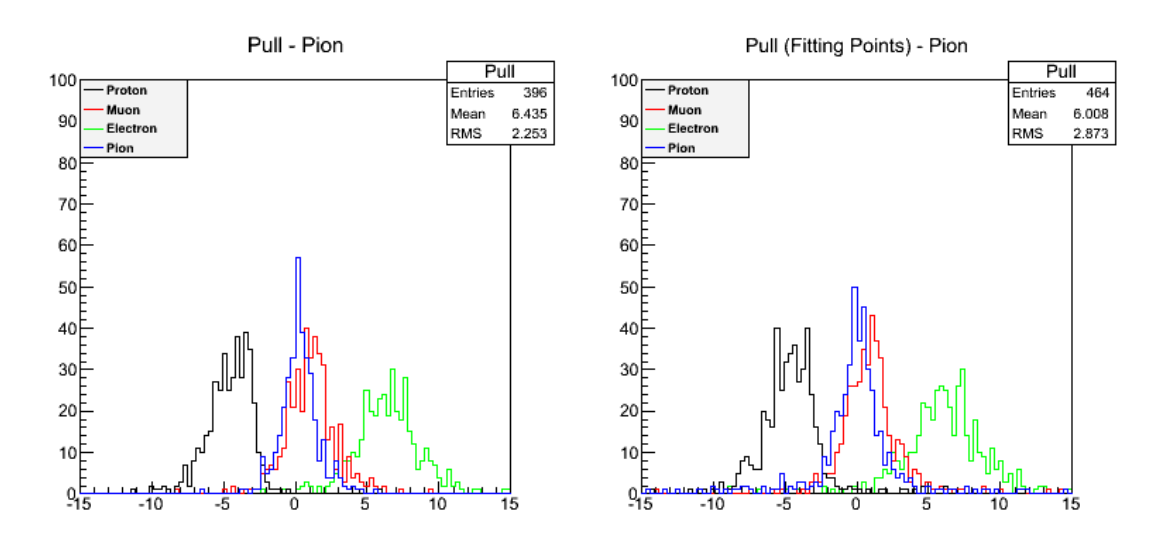


Figure 4.4: Pull distributions for each particle hypothesis assuming a pure pion sample in FGD1. (Original in colour.)

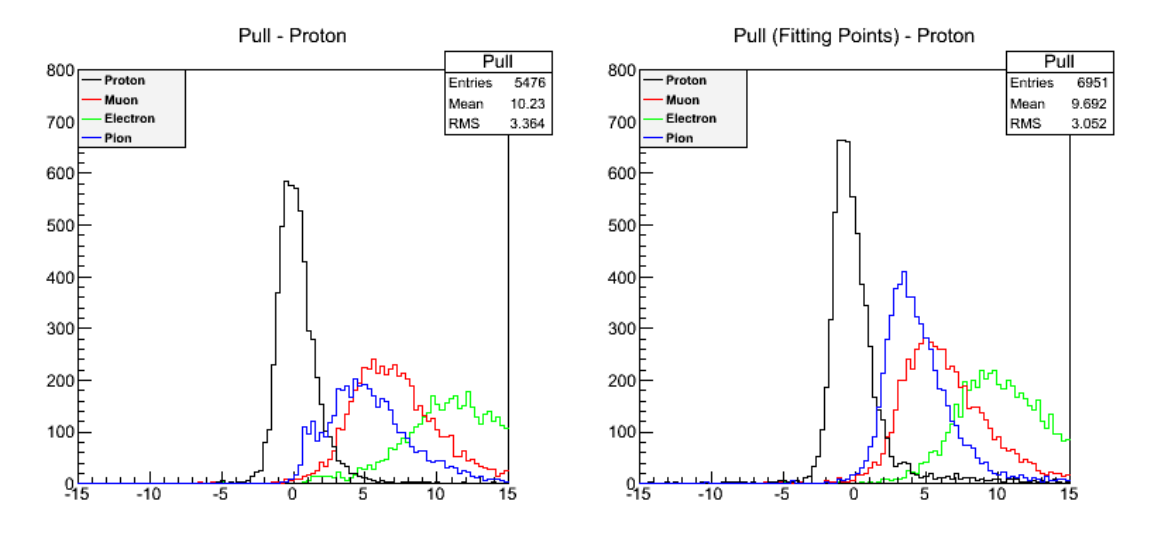


Figure 4.5: Pull distributions for each particle hypothesis assuming a pure proton sample in FGD2. (Original in colour.)

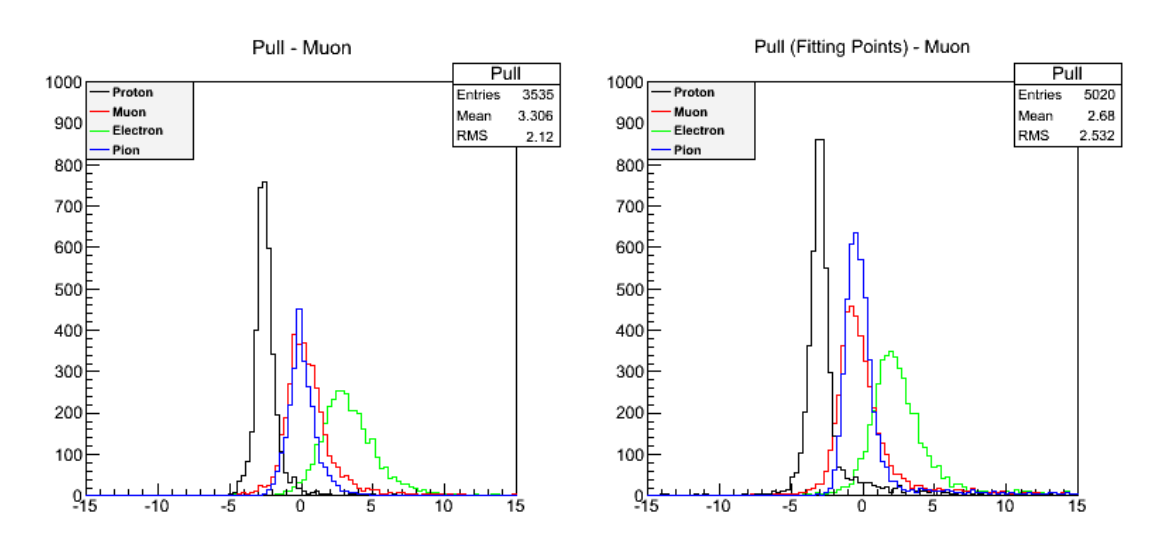


Figure 4.6: Pull distributions for each particle hypothesis assuming a pure muon sample in FGD2. (Original in colour.)

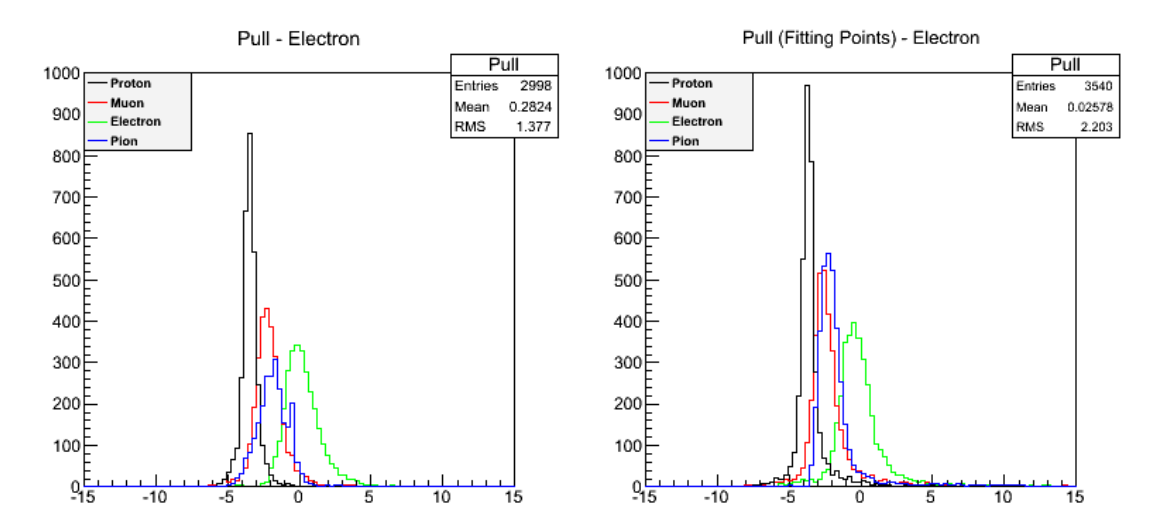


Figure 4.7: Pull distributions for each particle hypothesis assuming a pure electron sample in FGD2. (Original in colour.)

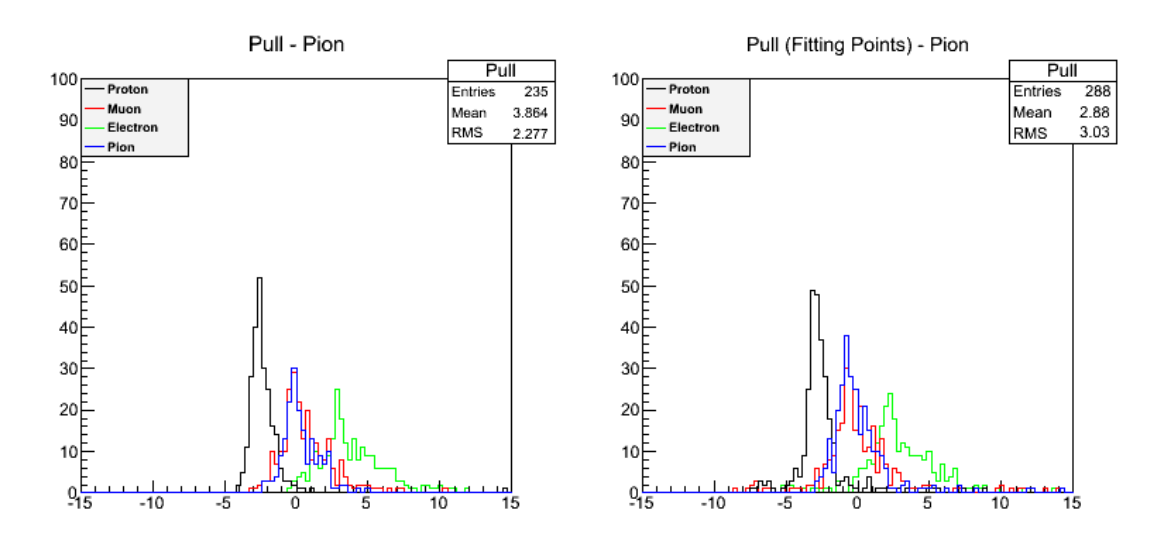


Figure 4.8: Pull distributions for each particle hypothesis assuming a pure pion sample in FGD2. (Original in colour.)

In both the fitting and table methods, the distributions for the correct particle hypothesis are closely peaked at zero, unlike those from the other (incorrect) particle hypotheses. In other words, both methods can be used to discriminate protons and electrons in a given sample. Pions and muons, on the other hand, cannot be individually

identified using either of these methods because the amount of energy deposited per track length unit is similar for both of these particle types, leading to similar pull distributions.

Since both table and fitting methods produce good results, the algorithm used for the PID is a combination of them, thus taking advantage of their qualities. The table method can sometimes lack points (no entries in some bins) in the distributions for the particles track lengths, but the fitting method allows the algorithm to extrapolate the curve to obtain values of energy for all bins of track length. In conclusion, the table method is chosen as the default in the final PID algorithm, with the fitting method used when a bin (or bins) of track length is (are) not present (empty bins) in the table method. The pull results from the combined method can be seen in fig. 4.9 for FGD1 and fig. 4.10 for FGD2.

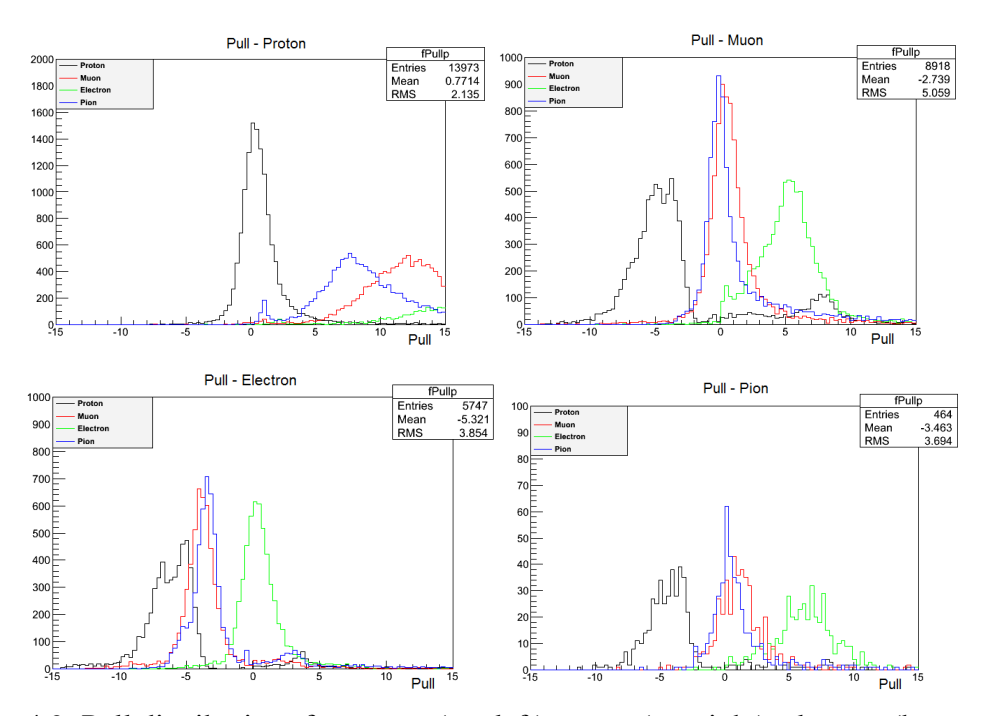


Figure 4.9: Pull distributions for proton (top left), muon (top right), electron (bottom left) and pion (bottom right) samples in FGD1 using the combined method. (Original in colour.)

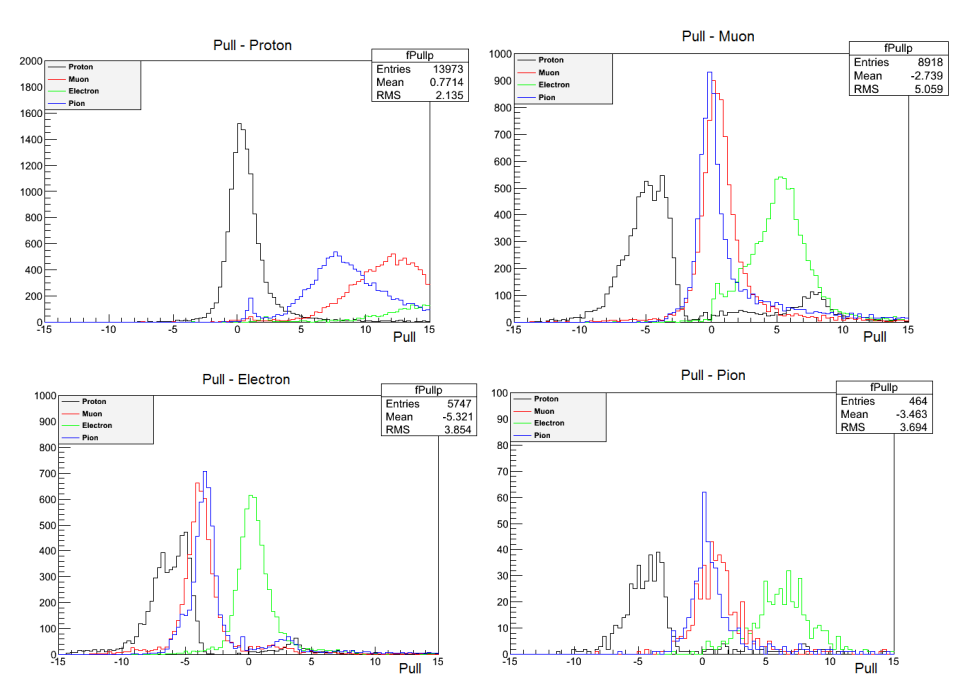


Figure 4.10: Pull distributions for proton (top left), muon (top right), electron (bottom left) and pion (bottom right) samples in FGD2 using the combined method. (Original in colour.)

The distributions from fig. 4.9 and 4.10 were fitted with Gaussian functions, and the eq. 3.6 was applied to calculate the likelihood for each particle hypothesis for each pure particle sample as described in section 3.5. The likelihood function is used to select the pull interval representing the region of higher probability of correct identification of a particle type in a given sample. The plots with the likelihood distributions as a function of the pull variables for FGD1 and FGD2 are shown in figs. 4.11 and 4.12, respectively.

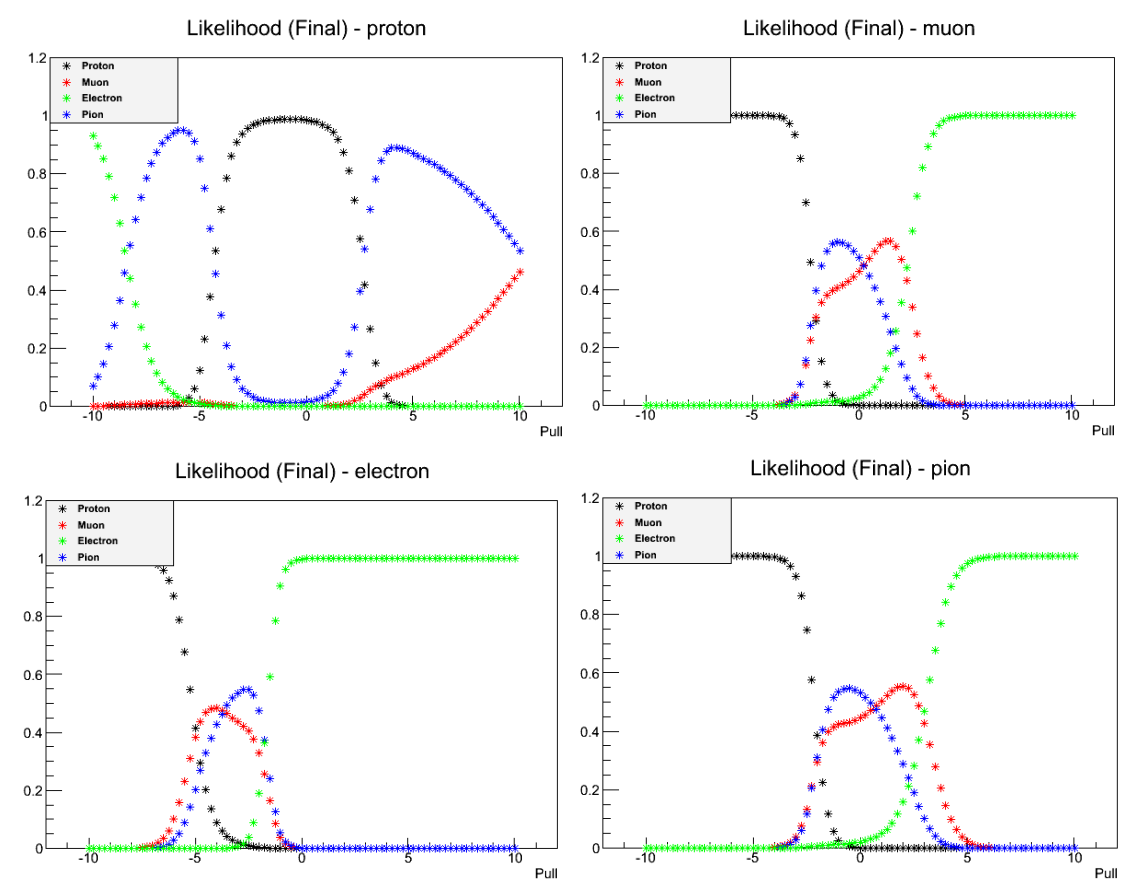


Figure 4.11: Likelihood for different particle hypotheses for sample of protons (top left), muons (top right), electrons (bottom left) and pions (bottom right) in FGD1. (Original in colour.)

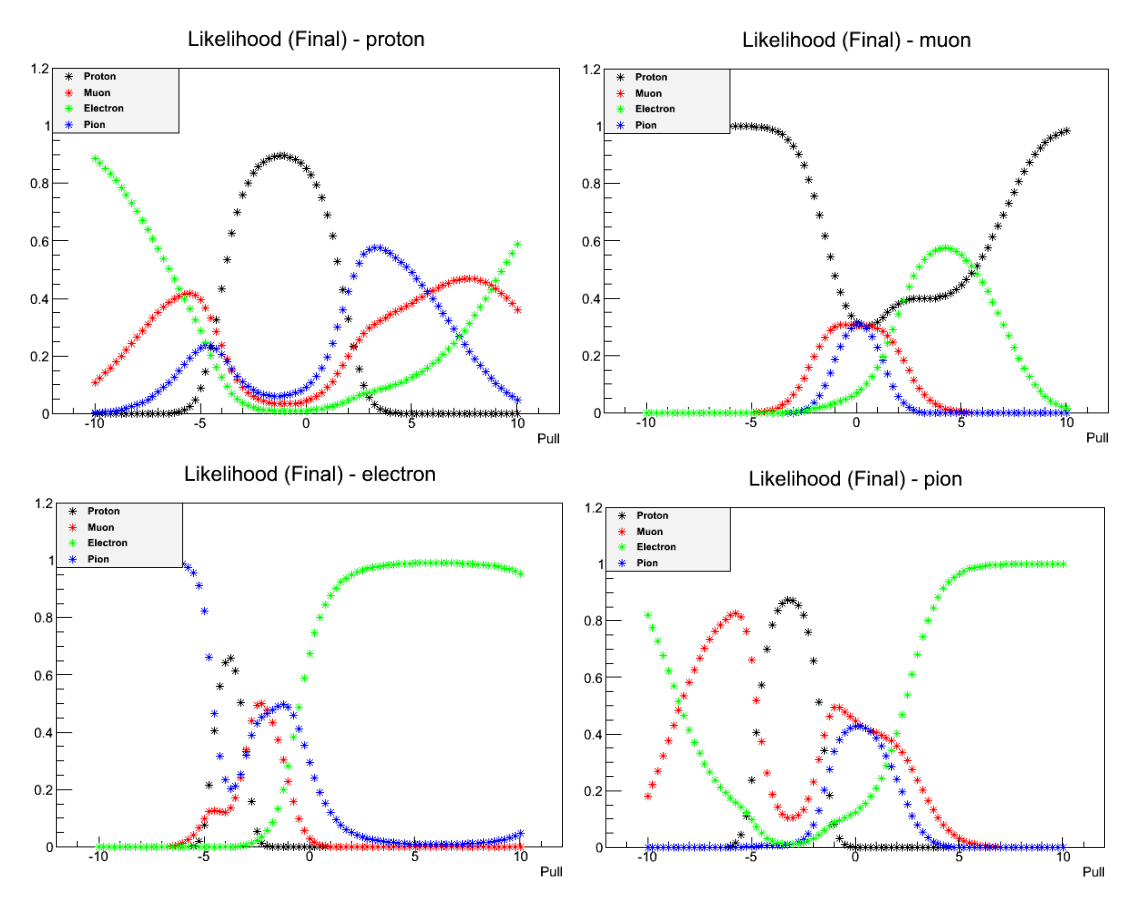


Figure 4.12: Likelihood for different particle hypotheses for sample of protons (top left), muons (top right), electrons (bottom left) and pions (bottom right) in FGD2. (Original in colour.)

## 4.2 Results using real data

To further test the PID algorithm, two sets of control samples, one of protons and another of muons, with real (non-simulated) data collected with the T2K experiment were used. These samples, with specific characteristics, were carefully collected and processed with the ND280 software by the T2K collaboration, and are available for different kinds of analyses and tests. The protons and muons in question are selected such that they stop within either one of the FGDs.

The proton control sample was selected from interactions between the neutrino beam particles and the ND280 detectors. The TPCs (see section 1.2 to recall what a TPC is) were used to identify and select protons, with following conditions to qualify the protons as stopping-protons:

- for a proton stopping in FGD1, the corresponding track has to present hits in TPC
   1, hits in FGD1 and not present hits in TPC 2.
- for a proton stopping in FGD2, the corresponding track has to present hits in TPC
   2, hits in FGD2 and not present hits in TPC 3.

Complications in this selection can arise when an event contains more than one reconstructed track (coming, for example, from multiple particle events or from a single track being reconstructed as more than one track due to the efficiency of reconstruction software). In these cases, the control sample algorithm will include those multi-track events when one of the tracks fulfills the criteria established above. In order to prevent including particles of other species in the proton control sample, or to prevent using events with bad reconstructed tracks, all events which contained more than one track have been excluded from this analysis.

The neutrino interactions producing the protons and muons selected in the control samples can take place outside the FGDs. On the other hand, the simulations used to construct the PDFs and pulls or the PID algorithm only assumes trajectories fully contained in the FGD. However, this fact does not pose any problem as, in cases where the protons or muons start outside the FGDs, one just has to consider the section of the trajectory starting in the first layer of either of the FGD detectors, and ignore the section of the track laying before that.

The pull distribution constructed using the PID algorithm for real (non-simulated) protons stopping in the FGD1 is depicted in fig. 4.13 and in fig. 4.14 for FGD2. It can be seen that the proton hypothesis best described the data (peak is closer to zero). The left and right side-tails in the distributions are due to impurities on the sample (despite the strict criteria employed in the selection of protons for the proton control sample, there is always some other particles that can be mistakenly selected and included in this sample).

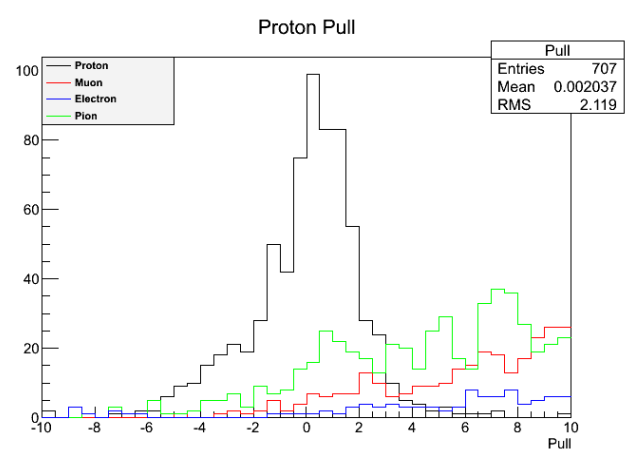


Figure 4.13: Pull distribution for proton, muon, electron and pion hypotheses when applied to stopping proton data sample in FGD1. (Original in colour.)

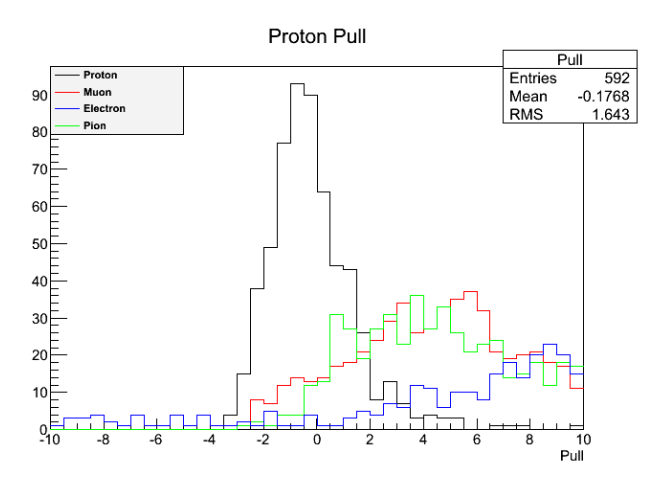


Figure 4.14: Pull distribution for proton, muon, electron and pion hypotheses when applied to stopping proton data sample in FGD2. (Original in colour)

Fig. 4.15 (FGD1) and fig. 4.16 (FGD2) show the comparison between the pull distributions obtained using real data (proton control sample) and simulated protons for the proton hypothesis. The agreement between the two types of distributions is very good.

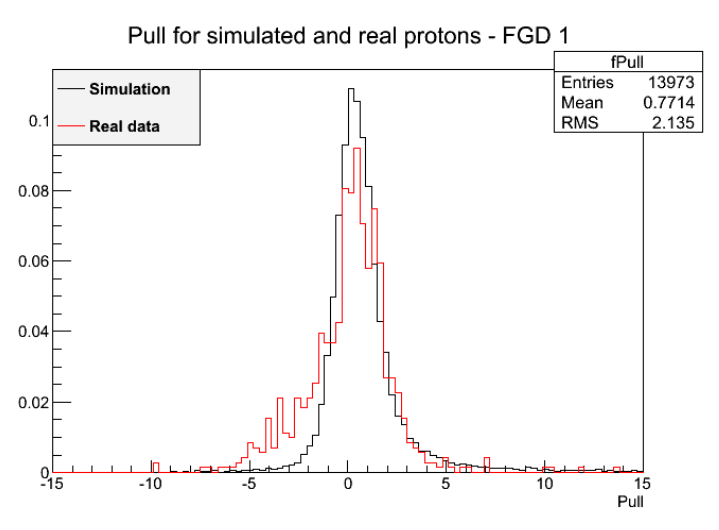


Figure 4.16: Comparison between pull distributions for simulated and real data assuming the proton hypothesis for FGD1. (Original in colour.)

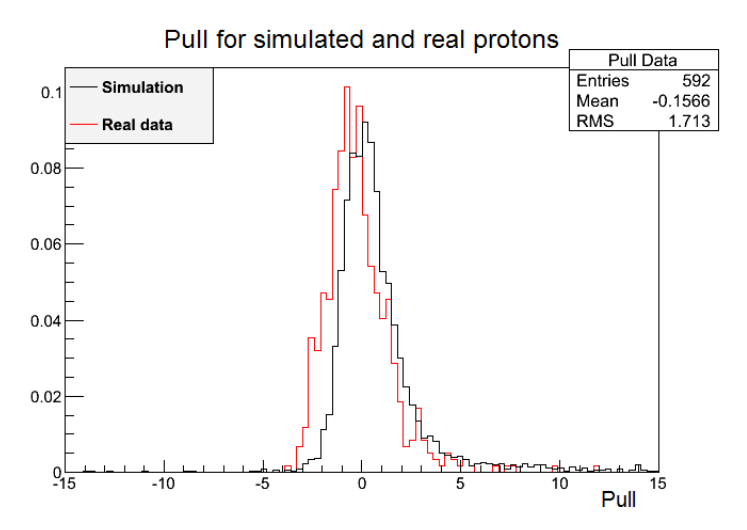


Figure 4.17: Comparison between pull distributions for simulated and real data assuming the proton hypothesis for FGD2. (Original in colour.)

The muon control sample was obtained from cosmic rays (the muons are produced by the interaction of cosmic rays with nuclei in the Earth's atmosphere, and are called cosmic muons due to their origin). The muon particles can cross the FGDs in either of the following directions: passing first through FGD1 and then through FGD2 (upstream), as the neutrino beam does; or the opposite way around (downstream). Because of the FGD Cosmic Trigger (the algorithm used by the FGDs to select cosmic events), that requires that a cosmic muon has to have hits in both FGDs, in horizontal and vertical bars, to be selected, the selection for stopping cosmic muons requires that the particle enters and exits one FGD and then enters and never exits the other. Therefore the selection criteria for these particles have to include both possibilities of directions and, therefore, are:

- for muons stopping in FGD1, the corresponding track has to present:
  - downstream-most and upstream-most hits in horizontal and vertical bars in FGD2.
  - downstream-most hits in horizontal and vertical bars in FGD1.
  - no hits within a distance smaller than 10 cm from the upstream edge in FGD1.
- for muons stopping in FGD2, the corresponding track has to present:
  - upstream-most and downstream-most hits in horizontal and vertical bars in FGD1
  - upstream-most hits in horizontal and vertical bars in FGD2
  - no hits within a distance smaller than 10 cm from the downstream edge in FGD2.

No further cuts were applied in the selection of the control sample in order to preserve a significant statistics necessary for this study.

The pull distribution for the real muons can be seen in figs. 4.18 and 4.19 for FGD1 and 2, respectively. Again, it is possible to see that the peaks for muons and pions are mostly coincident, as was discussed before, but that the separation between muon/pion and protons and electrons is clear, demonstrating once again, now with real data, that particle identification can be performed.

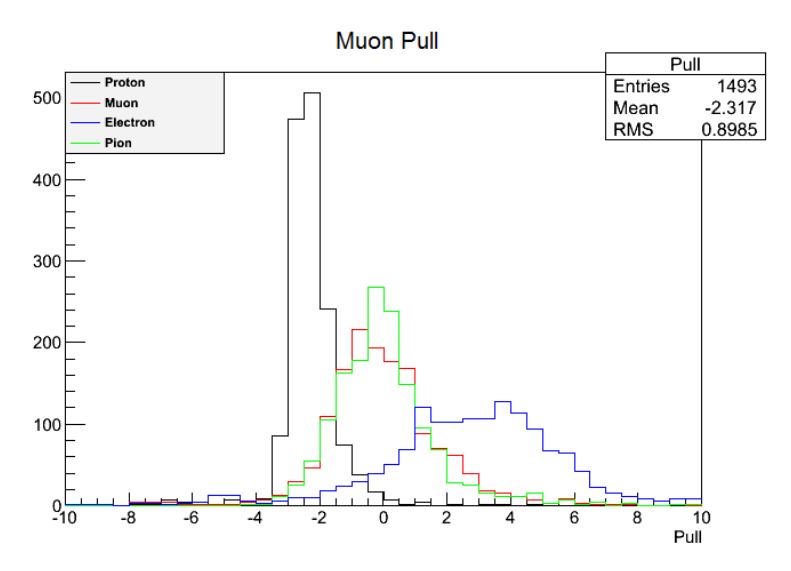


Figure 4.18: Pull distribution for proton, muon, electron and pion hypotheses when applied to stopping muon data sample in FGD1. (Original in colour)

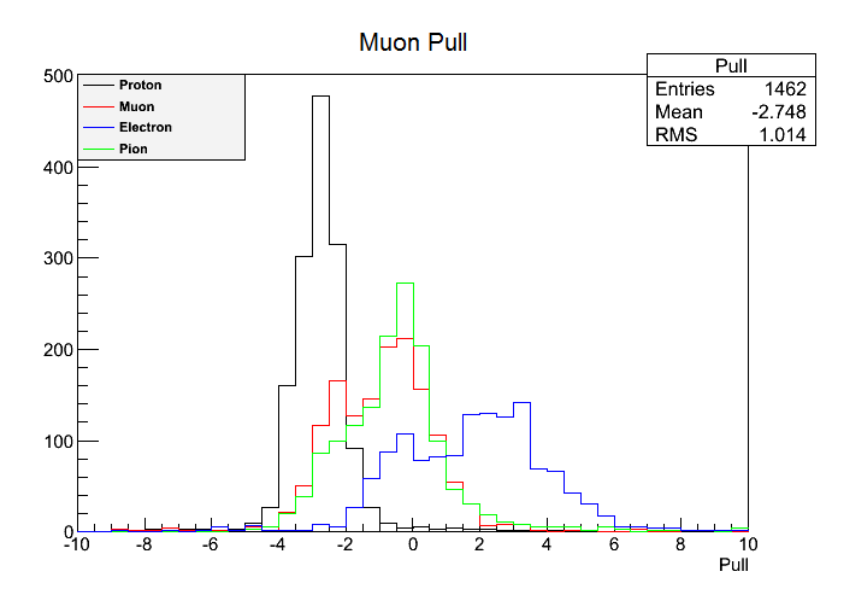


Figure 4.19: Pull distribution for proton, muon, electron and pion hypotheses when applied to stopping muon data sample in FGD2. (Original in colour)

As done for the proton control sample, fig. 4.20 (FGD1) and fig. 4.21 (FGD2) show the comparison between the pull distributions for simulated and real muons.

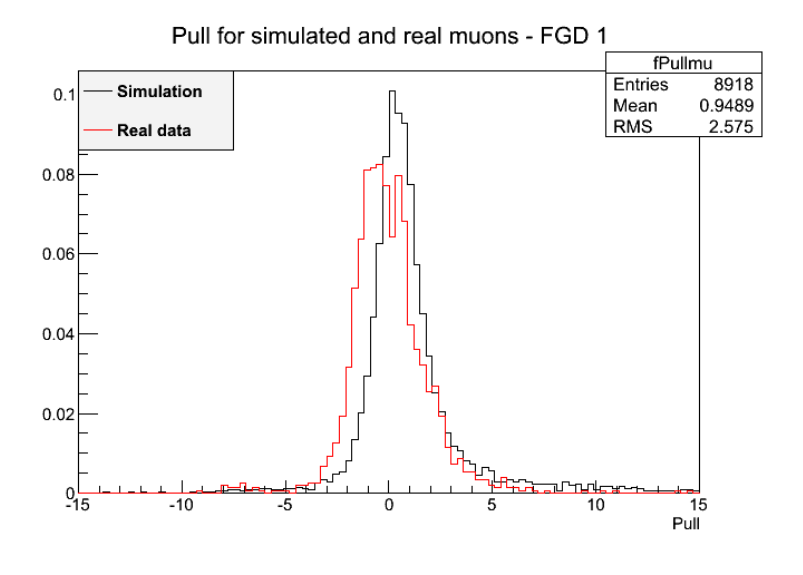


Figure 4.20: Comparison between pull distributions for simulated and real data using muon hypothesis and muon sample for FGD1. (Original in colour)

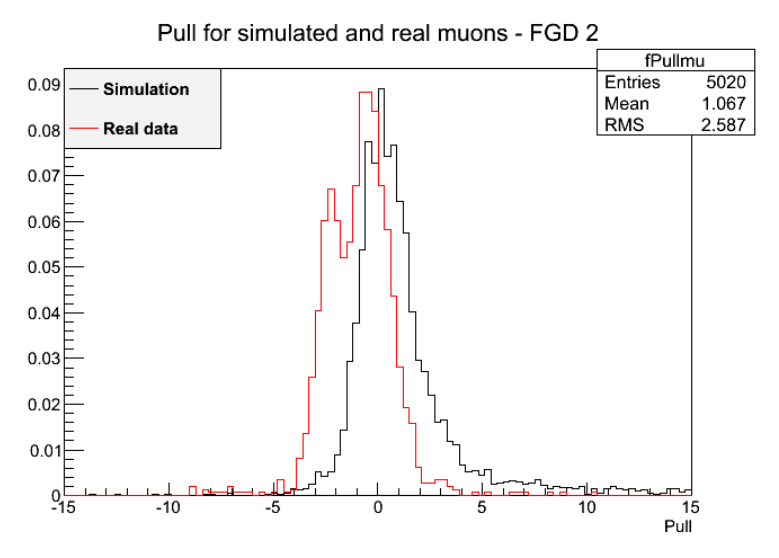


Figure 4.21: Comparison between pull distributions for simulated and real data using muon hypothesis and muon sample for FGD2. (Original in colour)

Apart from impurities in the real data sample, as can clearly be noticed in the real muon pull distribution for FGD2 (fig. 4.21), the results for real particles agree very well with the simulations, thus validating the PID algorithm.

## **CHAPTER FIVE: Conclusions**

The main objective of this thesis research was the development of a particle identification algorithm for FGD isotracks (tracks which start and stop within a FGD). During the research time, I also performed other activities for the T2K collaboration, as briefly described in Appendix A of this thesis.

The PID algorithm was developed based on two complementary methods: the table method and the fitting method (see section 3.4 for more details in both methods). The table method is used as the default framework for the PID, with the fitting method employed whenever no information is provided by the default method for certain given tracks. The algorithm was demonstrated to be able to identify proton and electrons in both simulated and real data with good efficiency for angles and energies between 0 and 70° and 0 and 500 MeV, respectively. Pions and muons are difficult to separate using the method implemented in the PID algorithm in the kinematic range analysed in this thesis. This is mainly due to the similarities between the energy deposition per track length between these two particles. Further work exploring alternate methods would have to be performed in order to accomplish the goal of significantly separating pions from muons.

Furthermore, the algorithm developed in this thesis modifies the previous FGD PID algorithm [30] in two ways: first, it introduces the identification of electrons. Second, it uses reconstructed simulated variables instead of true simulated variables when building the PDFs for protons, muons, pions and electrons. This allows a direct and more realistic comparison between the variables used to construct the pull variables, namely the predicted energy obtained from a given PDF hypothesis and the particle energy

reconstructed from the real data. Besides, the algorithm makes it easier for future developments such as the identification of particles exiting the FGD that do not leave enough hits in the TPCs for a proper identification with these detectors. In this sense, the FGD PID algorithm can be a valuable source of information even for events not fully contained in the FGDs.

The PID algorithm as described in this thesis has already been implemented in the general ND280 reconstruction algorithm and is fully functional, being already used to reconstruct the new T2K processed data.

## **BIBLIOGRAPHY**

- [1] D. Griffiths. *Introduction to Elementary Particles*. Second, revised edition. WILEY-VCH Verlag GmbH & Co. KGaA, (2008).
- [2] E. Fermi. Zeitschrift für Physik A 88 (3-4): 161 (1934).
- [3] A. Das, T. Ferbel. *Introduction to Nuclear and Particle Physics*. Second edition. World Scientific, (2003).
- [4] C. L. Cowan et al. Science 124 (3212): 103-104 (1956).
- [5] G. Danby et al. Phys. Rev. Lett. 9, 36-44 (1962).
- [6] M. L. Perl et al. Phys. Rev. Lett. 35, 1489-1492 (1975).
- [7] K. Kodama et al. [DONUT Collaboration] *Phys. Rev. B* **504** (3): 218-224 (2001)
- [8] K. Zuber. Neutrino Physics. Second edition. CRC Press, (2012).
- [9] J. Beringer et al (PDG). *Neutrino Mass, Mixing, and Oscillations*. PR D86, 010001 (2012) (http://pdg.lbl.gov).
- [10] F. Boehm, P. Vogel. *Physics of Massive Neutrinos*. Second edition. Cambridge University Press, (1992).
- [11] Q. R. Ahmad et al. Phys. Rev. Lett. 89, 011301 (2002).
- [12] Y. Fukuda et al. (Super-Kamiokande Collaboration). *Phys. Rev. Lett.* **81**, 1562 (1998).
- [13] K. Abe et al (The T2K Collaboration). Phys. Rev. Lett. 112, 061802 (2014).
- [14] F. P. An et al. *Phys. Rev. Lett.* **108**, 171803 (2012).
- [15] T2K Experiment. What We Know. Available on: "http://t2k-experiment.org/neutrinos/oscillations-today/" (Sep. 14<sup>th</sup>, 2013).

- [16] K. Abe et al (The T2K Collaboration). Nucl. Instrum. Methods Phys. Res. Sect. A 659, 106 (2011).
- [17] A. K. Ichikawa. Nucl. Instrum. Methods Phys. Res. Sect. A 690, 27 (2012).
- [18] P. Amaudruz et al. (T2K ND280 FGD Collaboration). *Nucl. Instrum. Methods Phys. Res., Sect. A* **696**, 1 (2012).
- [19] Hamamatsu. *MPPC*, *MPPC Modules (technical information)*. Available on: "http://www.hamamatsu.com/resources/pdf/ssd/mppc\_techinfo\_e.pdf" (Jun. 19<sup>th</sup>, 2014).
- [20] M. Yokoyama et al. arXiv:1007.2712.
- [21] B. R. Martin, G. Shaw. *Particle Physics*. Second edition. John Wiley & Sons, (1997).
- [22] Bethe, H. Ann. Phys. **397**, 325–400 (1930).
- [23] Bloch, F., Ann. Phys. 408, 285–320 (1933).
- [24] A. Mozumder, Y. Hatano. *Charged Particle and Photon Interactions with Matter*. Marcel Dekker, Inc., (2004).
- [25] K. F. Johnson. *Particle Detectors at Accelerators: Organic Scintillators*. Revised August 2011. Available on: "http://pdg.lbl.gov/2013/reviews/rpp2012-rev-particle-detectors-accel.pdf".
- [26] J. B. Birks. *Proc. Phys. Soc. A* **64** 874 (1951).
- [27] A. Hillairet et al. T2K-TN-072. (Internal T2K note).
- [28] S. Agostinelli et al. Nucl. Instrum. Methods Phys. Res., Sect. A 506, 250 (2003).
- [29] R. E. Kalman. J. Fluids Eng. 82, 35-45 (1960).

[30] C. Licciardi. Measurement of Single Positive Pion Production in Neutrino Neutral Current Interactions in the ND280 Detector and Particle Identification with the Fine Grained Detector at T2K. PhD Thesis. University of Regina, (2012).

## APPENDIX A

## Other contributions for T2K

During the research time, I also performed other activities for the T2K collaboration, which will be briefly explained in the next paragraphs.

Firstly, I worked in the calculation of FEB-to-FEB (front-end board) offsets in the FGDs. These offsets refer to the differences in hit timing among the FGD FEBs. They needed to be adjusted to a new version of the software. My work was to calculate the offsets of all FEBs relative to an arbitrarily chosen one and then apply the corrections in the software.

I also worked as FGD on call detector expert in Japan for two months, where I was responsible for dealing with any problems in FGD during that time to guarantee the detector was running the most amount of time possible for data taking.

The last job I had in the collaboration was as FGD data quality expert for a little longer than a year. In this case, I was responsible for analysing the data quality plots for FGD and verify no problems happened in the detector while data was being collected. I also had to flag if the quality of data was good or not in the data quality database.